2011

Lineament mapping for groundwater exploration using remotely sensed imagery in a karst terrain : Rio Tanama and Rio de Arecibo basins in the northern karst of Puerto Rico

Carla A. Alonso-Contes
Michigan Technological University

Recommended Citation

Alonso-Contes, Carla A., "Lineament mapping for groundwater exploration using remotely sensed imagery in a karst terrain : Rio Tanama and Rio de Arecibo basins in the northern karst of Puerto Rico", Master's Thesis, Michigan Technological University, 2011.
https://doi.org/10.37099/mtu.dc.etds/309

Follow this and additional works at: https://digitalcommons.mtu.edu/etds
Part of the Geology Commons, and the Geomorphology Commons

LINEAMENT MAPPING FOR GROUNDWATER EXPLORATION USING REMOTELY SENSED IMAGERY IN A KARST TERRAIN: RIO TANAMÁ AND RIO DE ARECIBO BASINS IN THE NORTHERN KARST OF PUERTO RICO

By
Carla A. Alonso-Contes

A THESIS

Submitted in partial fulfillment of the requirements for the degree of

MASTER OF SCIENCE

(Geology)

MICHIGAN TECHNOLOGICAL UNIVERSITY

2011

This thesis, “Lineament Mapping for Groundwater Exploration Using Remotely Sensed Imagery in a Karst Terrain: Rio Tanamá and Rio de Arecibo basins in the Northern Karst of Puerto Rico,” is hereby approved in partial fulfillment of the requirements for the Degree of MASTER OF SCIENCE IN GEOLOGY

Department of Geological and Mining Engineering and Sciences

Signatures:

Thesis Advisor ______________________________
Dr. John S. Gierke

Department Chair ______________________________
Dr. Wayne D. Pennington

Date ______________________________

This thesis is dedicated to Ma, Pa, Andrés A. and Ivana P.

Table of Contents

List of Figures

List of Tables

Acknowledgements

This research is supported by the US National Science Foundation through OISE and PIRE 0530109.

I am very grateful to my advisor John Gierke for indefinite support, helping be grow as a person, and as a graduate student and for giving me the opportunity to do research at Tech when I was still an undergraduate at UPRM. I would like to express my gratitude to my committee members Ann Mclean, for answering all of my questions regarding GIS and helping me become more proficient in ArcGIS. I would like to give many thanks to Mike Falkowski for all the support regarding remote sensing applications and data acquisitions and processing. Thank you, Tom Miller and Simon Carn, for answering all my questions throughout this process. Gracias Lizzette Rodriguez for your unconditional help, you were my first mentor and you motivated me to come to Tech and pursue a graduate career. Gracias Miriam Rios for being my friend and mentor in hydrogeology, remote sensing, and life. Briana Drake for being my friend and the best field assistant one could hope for. I'm extremely grateful to Essa Paterson and Jill Bruning for your friendship and for letting help them in their research I have always looked up to you two. Finally, Roger and my family (mom and dad specially) and friends for support and love you are my backbone and my motivation to keep going.

Abstract

Remote sensing and advanced digital image processing techniques were developed and tested for delineating karst features important for the subterranean hydrology in the Tanamá River and Rio Grande de Arecibo catchments located in the North Coast Tertiary Basin of Puerto Rico, where groundwater contributes to base flow for surface water bodies which in itself is the main supply of drinking water. This aquifer region is a karst platform of carbonate rocks and clastic beds, thought to comprise a confined aquifer beneath and an unconfined aquifer. Products derived from ASTER, Landsat (ETM+ and TM), a NED DEM (30 m), and a LiDAR DEM (2 m) were analyzed in the interpretations of the karst flow system. In addition, field verification, VLF-EM, and previously published hydrologic data were analyzed to characterize fracturing and dissolution features on groundwater hydrology in the region. Remote sensing assessments show that Landsat PCA (incorporating thermal band,) ASTER PCA, LiDAR Hillshade were best at detecting “true” lineaments in this type of terrain. NDMI proved to be helpful in detecting moisture changes attributed to lineaments influencing the shallow hydrology in the karst. Geomorphic data agrees with lineaments as faulting and fracturing in addition to linear bedding control features. Sinkholes, springs and geotectonic evidence locations occur along and at the end of lineaments. Lineaments interpreted from LiDAR DEM data (Aspect, Hillshade) show regional geomorphotectonic evidence correlated to sharp river bends, hill alignment, and aspect trends.

1. Introduction

Current methods for analyzing remote sensing data to delineate fractures and discontinuities in hard-rock terrains could be used to improve water-well-siting strategies. Groundwater recharge and/or discharge zones may be detected using satellite remote sensing techniques that enhance temperature, vegetation, and water content variations (Meijerink et al. 2007). Geomorphotectonic features (e.g., bedding planes, foliations, and faults) occur as linear features (i.e., lineaments), which can be detected by remotely sensed imagery. Bruning et al. (2011) demonstrated how lineaments could be detected and digitized using remotely sensed imagery by identifying contrasting pixel patterns in imagery from a small (66 km^2), highly weathered, volcanic region in Nicaragua, where the landscape has been significantly altered by anthropogenic activities. Rios-Sanchez et al. (in Preparation) is further advancing the work of Bruning et al. (2011) for a large, complex volcanic sedimentary basin in Ecuador. The work described in this thesis is aimed at developing a similar approach for karst terrains.

Common applications of remote sensing images in karst terrains are the mapping of features as indicators of dissolution of the rock (Rinker 1974; Benson and Yuhr 1993). Other applications include mapping faults, lineaments and discontinuities that can be associated with cavern/fissure conduits, and mapping regional faults that can be associated with zones of high permeability and concentrated groundwater flow (Meijerink et al. 2007).

Geological lineaments can be of structural or geomorphologic origin and when viewed by certain satellite sensors exhibit drainage or vegetative influences and which must be differentiated from anthropogenic effects such as roads, trails, and fence lines. They are expressed in the form of texture, color and topographic changes. This thesis documents a variety of methods to enhance such features for karst terrain and the image-selection process for maximizing the information most important for hydrological characterization, based on the approach first developed by Bruning (2008).

1.1. Remote Sensing

Remote sensing (RS) imagery and derived products, such as Digital Elevation Models (DEMs), RADARDAT-1, Landsat TM & ETM+ and ASTER, have been widely used for mapping geological lineaments (Bruning et al. 2011) pertaining to major fault zones and generally to assess the degree of fracturing of those geological units (Edet et al. 1998) for groundwater applications (Kresic 1995; Sander et al. 1997; Tam et al. 2004; Hung et al. 2005; Kazemi et al. 2009). For this study, I was interested in using remotely sensed imagery with different spectral, spatial and radiometric resolutions to explore their value in identifying surface expressions of karstic features.

Various digital image processing (DIP) techniques have been shown to be useful for enhancing the appearance of lineaments in satellite images of volcanic areas (Bruning et al. 2011), such as principal component analysis (PCA), decorrelation stretch, edge enhancement filters, and others. Original images used for this study include: Landsat ETM+ (30 m spatial resolution) and the Panchromatic band (15 m), ASTER visible bands (15 m), Light Detection and Ranging(LiDAR) DEM (2 m) and a RADARSAT-1 image with ascending (12.5 m) and descending orbits (50 m). The use of different types of imagery, along with products derived from them through DIP, can enhance the appearance of features on the earth surface. Moreover, with the use of radar imagery and DEMs, geomorphologically influenced drainage patterns can be identified. Such geomorphic features (i.e., alignments of valleys or other features as hill or stream segments) can be identified as lineaments (Hung et al. 2005). In addition, as (Bruning et al. 2011) suggested, geophysical surveys can be conducted to complement satellite Remote sensing (Ramli et al. 2009). For example, very-low frequency (3 kHz to 30 kHz) electromagnetic (VLF-EM) surveys have been used for hydrogeological studies (Guérin 2005).

1.2. Karst and Lineaments

Water, high temperatures, and geological structure contribute to the formation of tropical karst topography and hence affect their susceptibility to contamination and water-supply development. Absorption of CO_2 in precipitation, which eventually recharges groundwater, causes dissolution of limestone. Limestone porosity is increased from dissolution by water moving through joints and bedding planes, eventually creating conduits and caves. Groundwater in karst terrain has an irregular water table, making monitoring and characterization complicated tasks.

Karst topography is mostly characterized by sinkholes. Caves are also common in karst topography and develop due to higher groundwater flow and depend on structure and recharge/discharge points. Geographic location of these features may often seem arbitrary but upon broader perspective can be found to originate and grow along joint strikes or bedding planes (Easterbrook 1999).

Lineaments extracted from RS imagery, topographic and geologic maps, and other sources have been used for groundwater studies (Bruning et al. 2011). A lineament, for this study, is defined as a linear feature corresponding to faulting, fracturing, geomorphologic feature or vegetation trends due to groundwater recharge/discharge zones (Meijerink et al. 2007). These features might be indicators of rock solubility and can be associated with cavern/fissure conduits. Bruning et al. (2011) demonstrated how lineaments could be mapped using satellite imagery by visually detecting contrasting color, tone and texture patterns in a volcanic region. Applying these previously developed techniques and adjusting as needed for characterizing karstic terrains could help to understand the groundwater flow systems.

A common application of remote sensing images in karst terrains is the mapping of features as indicators of rock solubility. This information can be related to the underground karst network. Other applications include mapping faults, lineaments and discontinuities that can be associated with cavern/fissure conduits and mapping faults that can be associated with zones of high permeability and concentrated groundwater flow (Meijerink et al. 2007). Groundwater discharge zones may be identifies along coastal swamps and lagoons (Giusti 1978; Jones et al. 2000). Recharge in karst areas is mostly characterized by infiltration through hydrological/germorphological features found in karst (e.g. sinkholes intermittent streams and valleys) (Kresic 1995; Jones et al. 2000; Salvati and Sasowsky 2002). Another application for lineament mapping is in characterizing the susceptibility of landscapes to sinkholes formation (Giusti 1978; Salvati and Sasowsky 2002; Koutepov et al. 2008) and groundwater contamination (Yilmaz 2007). The method proposed herein can be used to map collapse hazards that are greatly influenced by faulting (Yilmaz 2007) .

In addition to similar optical and radar imagery used in Bruning et al.(2011) (with exception of the Quickbird image), Landsat TM & ETM+ thermal bands and a high-resolution LiDAR DEM are used in this work. Furthermore, in addition to enhancement of relief changes due to faulting in limestone , thermal imagery can show sharp temperature contrasts, which could be due to groundwater discharge through major faults or ground water presence and evapotranspiration (Meijerink et al. 2007). Shaban et al. (2006) made use of the Landsat ETM+ thermal band in addition other bands for pinpointing wet areas (cooler), which were attributed to fracture zones. Results from this study showed that a higher density of lineaments cause higher recharge potential. Offield (1975) used airborne thermal images from two different times of day to delineate topographical lineaments corresponding to major faults or stratigraphic boundaries.

To have a better representation of the surface topography of this highly vegetated area, a LiDAR DEM was utilized in this study. LiDAR data provides a good representation of the topography because LiDAR pulses will pass through the gaps in vegetation to provide ground elevation measurements (Korpela 2008). Remmel et al (2008) used a LiDAR DEM and derived data such as slopes and surface aspect to delineate surface hydrologic features (low order springs, watershed boundaries and depressions) for hydrogeological modeling. Despite the previous applications of LiDAR in hydrology, ground truthing LiDAR and other remote sensing data still remains crucial (Hawbaker et al. 2009). LiDAR-derived DEMs allow us to have a clearer view of the topography for applications such as landslides, inundation, sinkholes (Carter et al. 2001), faulting, infiltration and runoff (Harding and Berghoff 2000; Haugerud et al. 2003) compared to aerial photography (Haugerud et al. 2003). Begg and Mouslopoulou (2010) used LiDAR to measure displacement rates and identify geomorphic features along a fault scarp in volcanic terrain in the Taupo Rift, New Zealand. These features were represented as lineaments in the DEM. Sherrod et al.(2004) also used LiDAR to map lineaments corresponding to fault scarps for measuring uplift.

Hung and Batelaan (2003) utilized Landsat ETM+ (including the panchromatic band), change detection analysis and a PCA to delineate recharge and discharge zones to identify dry and wet areas. The authors also used the image and additional edge enhancements to extract lineaments automatically using Line module of PCI Geomatica software to construct lineament density maps. Normalized Difference Vegetation Index (NDVI) was used to make unsupervised classification maps of land cover. Also, Hung et al. (2002) found that lineaments have a strong correlation to cave development.

Sankar (2002) used IRS LISS-III imagery to manually delineate lineaments, geomorphic features (residual hills, weathering deposits along foothills and floodplains) and well yields to determine groundwater potential zones. Their results showed lineament-intersection locations as potential zones for groundwater supply development. Kazemi et al. (2009) used Landsat ETM + imagery, aerial photography, geologic maps, and a DEM to map zones of potential karst development and found that the presence of a spring can be related to contact between karst and non-karstic rock and other tectonic features. Generally the authors found that springs mostly occur at closer distances to lineaments.

Hung et al. (2005) compared different spatial resolution images from two sensors (Landsat ETM+ and ASTER) for their ability to identify lineaments through automatic extraction using the Line module of PCI Geomatica in addition to Landsat ETM intensity–hue–saturation (IHS) fusion. ASTER & Landsat ETM+ fusion products were also evaluated and it was determined that ASTER VNIR bands produced the most detailed and accurate lineament map. Their results showed that known fracture zones lay near high lineament density areas.

Tam et al. (2004) found a correlation between lineament density extracted from automatically using Geomatics PCI line module with Landsat ETM+ , Landsat ETM+ PCA, manually extracted lineaments from an black and white aerial photographs and specific capacity (Sc) of boreholes. In addition, they found that even though lineaments might be buried under quaternary deposits they still affect hydrology. Higher Sc values were located near river systems (discharge zones).

Sesôren (1985) joined coinciding manually extracted lineaments of various (infrared and black & white) composites of Landsat MSS images into one lineament map. The author concluded that more regional lineaments are covered under the travertine plateaus and show up as subtle linear expressions on the surface. Therefore, the subtle expressions could be continuations of regional fractures or faults that are expressed in the surrounding area. Their results showed that lineaments correlate to the presence of shallow depressions and sinkholes caused by groundwater dissolution of fractures. Kresic (1995) used Landsat imagery and aerial photographs to attribute sinkhole orientation to a preferred faulting direction.

Ramli et al.(2009) used Landsat TM, Landsat ETM+ and a DEM to find lineaments manually by visual interpretation on a tropical densely vegetated environment in Malaysia. Processing included Fusion of Lansdsat ETM false color image with the panchromatic band as well as use of a linear contrast stretch on Landsat TM bands753. Field campaign included joint, dip and dip direction and foliations measurements. They also incorporated river drainage patterns to their comparison with interpreted lineaments. Results show good correlation between river segments, field data and remote sensing imagery lineament orientation. To reduce subjectivity the authors had the interpreter take a second look to the lineament map two months after the original lineament was digitized. They also suggest the uses of more than one interpreter.

Additional automatic lineament extraction techniques include work by the following:

Koike et al.(1995) used a Segment Tracing Algorithm (STA) in order to minimize sun illumination and shadow effects on lineament extraction.
Lee and Moon (2002) used the Hough transform algorithm. Satellite imagery needs to be pre processed with a linear edge enhancement method and then converted in to binary format prior to the use of this algorithm.

Vassilas et al.(2002) used a modified Hough transform to automatically extract lineaments on a binary image from Lansdat TM. They also incorporated manually interpreted lineaments by an expert interpreter to compare results from both techniques. They found that the automatic method better detected perfectly linear features as opposed to more curvilinear lineaments. Some lineaments were found using in both methods. Karnieli et al.(1996) also used this method on the geologically unique environments. Their results matched with previously manually digitized lineaments.

Kocal et al.(2004) also used LINE module of PCI Geomatica v8.2 for automatic lineament extraction. In addition, manual on screen digitations on directional filters was also carried out as a reference to determine the accuracy of the automatically extracted lineaments. Prior to the comparison between manual and automatic roads had to be deleted, as well as those lineaments outside of the study area. The authors determined that manually digitizing lineaments permit a better method to discern man made and non-geological lineaments.

Wladis (1999) used a second vertical derivative filter to automatically extract lineaments of a DEM. When results were compared to previous lineament maps the method showed to be inappropriate to detect a curvilinear and “step like” or broad valley lineaments.

While there are many studies on lineaments done using various automatic methods, manual on screen digitizing of lineaments is the preferred method for this study. Manually digitized lineaments may be time consuming and to an extent subjective, it still shows to be a better method to detect lineament type (geologic origin and vegetation trends vs man made) (Wladis 1999; Kocal et al. 2004; Hung et al. 2005; Ramli et al. 2009). The removal of such non geological lineaments from a automatically developed lineament map it can also be time consuming (Wladis 1999) as well as the preprocessing prior to filtering. Choosing the algorithm or filtering threshold and parameter values may also prove to be subjective in nature (Wladis 1999).

Most studies agree that geomorphological features must be taken into account when mapping lineaments groundwater. However, the exact nature of these features is dependent on the area (degree of karstification and other geological features that are present). Nevertheless, the important features to look for are: alignment of hills and valleys and river segments, topography, abrupt elevation changes, drainage patterns, geologic contacts (Della Seta et al. 2004) and other hydrologic data, such as spring locations, well yields, and water table elevations. The common remotely sensed data, products and processing techniques used for these purposes in karst include ASTER VNIR band, PCA, Normalized Difference Moisture Index (NDMI), edge filters, elevation analysis, among many others. No one data type or processing methodology is useful under every condition (cf.Bruning et al. 2011 and; Rios-Sanchez et al. in Preparation) Also radar can be used for regional feature identifications (Edet et al. 1998). Ward et al. (1991) mapped lineaments on a geologic map of the main limestone formations of the northern karst system shown in Lineament Analyses Section 4.1.

In this work, I am complementing RS techniques similar to those explained above with VLF-EM data. Geophysical techniques have been used for fracture networks affecting groundwater studies (Rios-Sanchez et al. in Preparation) Djeddi et al. (1998) used Fraser filtering of VLF-EM data to characterize dimensions of subsurface structures to determine depths and extent of fracture zones.

1.3. Study Location

Puerto Rico is located in the Caribbean Sea, southeast of the Southern Florida Coast. The area of study is located in the Northwestern part of the island, in the Tanamá river catchment. The area belongs to the so–called Northern Coast Karst (NCK) belt, the extent of which is depicted in Figure 1.1 and a part of which is shown from an aerial perspective in Figure 1.2. The NCK Basin of Puerto Rico accounts for 22% of the freshwater withdrawals on the island and it is also incorporated as base flow in surface hydrology (Lugo et al. 2001) and is an important habitat for a wide variety of flora and fauna. Due to its rough terrain there is little (practically none) development.

The NCK is made up of several karst formations. Karst aquifers are one of the main sources of potable water and irrigation for the Northern part of Puerto Rico and for other areas in the Caribbean. However, exploitation and lack of management of these sources has occurred due to poor knowledge of the hydrogeology. This has caused an imbalance in the hydrogeological system, leading to exhaustion of water sources, pollution, saltwater intrusion, and ground subsidence, among other issues. In addition, government support for mitigation is inadequate and contaminated aquifers are often abandoned (Hunter and Arbona 1995).

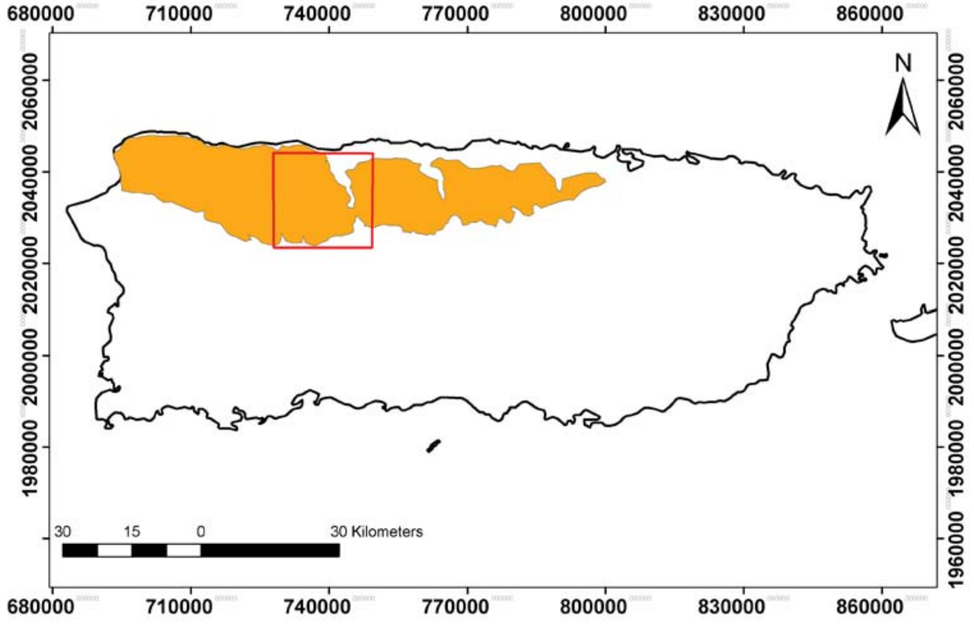

Figure 1.1 Location map of the study are enclosed in red. The extent of the Northern Karst System is shown in orange digitized and adapted from Alemán González (2010)

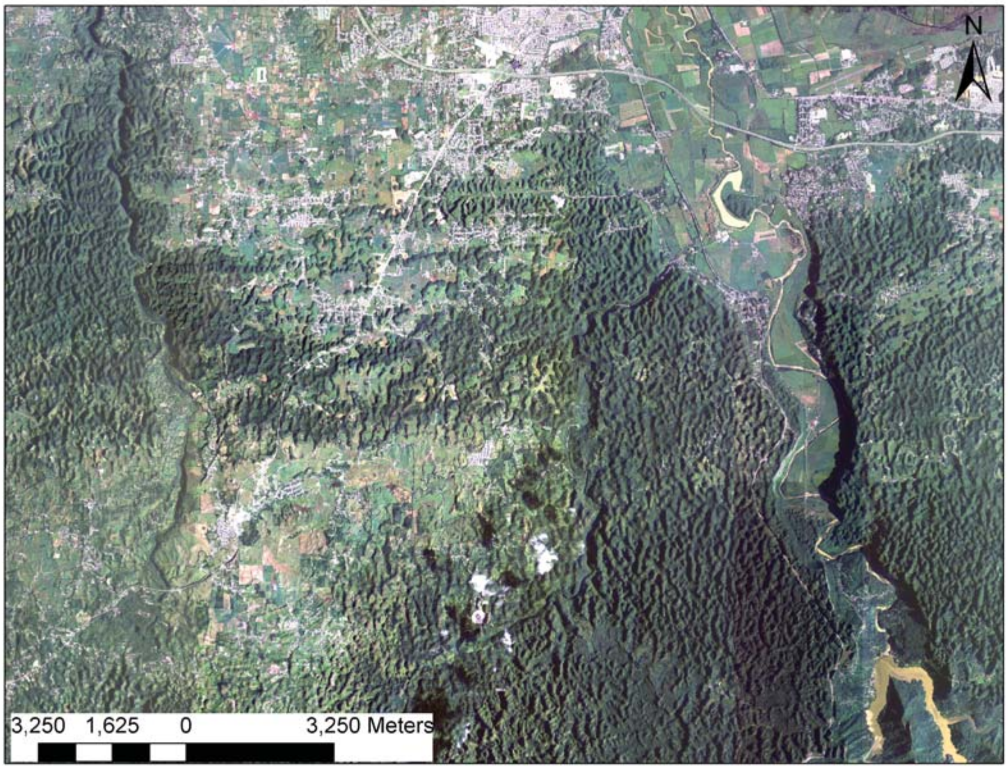

Figure 1.2 Ortho-photo (1-m resolution) of the study area extent from USGS.

The Puerto Rican North Coast Tertiary Basin (Figure 1.3 & Figure 1.4) has 2000 m of accumulated carbonate and siliclastic sedimentary rock from the Oligocene and Pliocene (Renken et al. 2002). These units dip to the north and strike east-west. Additional description of geologic units are fully described by Bawiec (1998) and Alemán González (2010). This aquifer region is a karst platform of carbonate rocks and clastic beds of two separate aquifers, a confined aquifer underlying an unconfined aquifer. This causes the groundwater to flow down dip along the more permeable bedding layers (Giusti 1978).

Climate is a factor that influences recharge, so it is vital to have knowledge of what are the seasons for this area of study. The rainy season occurs in June through November, especially from August through November when 60% of annual rainfall takes place in Puerto Rico. Discharge of groundwater usually happens along the coast into the sea or swamps and lagoons (Giusti 1978). The preponderance of springs on the western sides of river valleys could be partially explained by the effect of the eastward tilting of the PR platform (Giusti 1978; Rodriguez-Martinez 1997) but the presence of many (but fewer) springs on the opposite side of the river dispute this generalization (Rodriguez-Martinez 1997). Permeability contrasts between successive geologic units appears to be the main factor controlling the occurrence of springs in the NKB (Rodriguez-Martinez 1997).

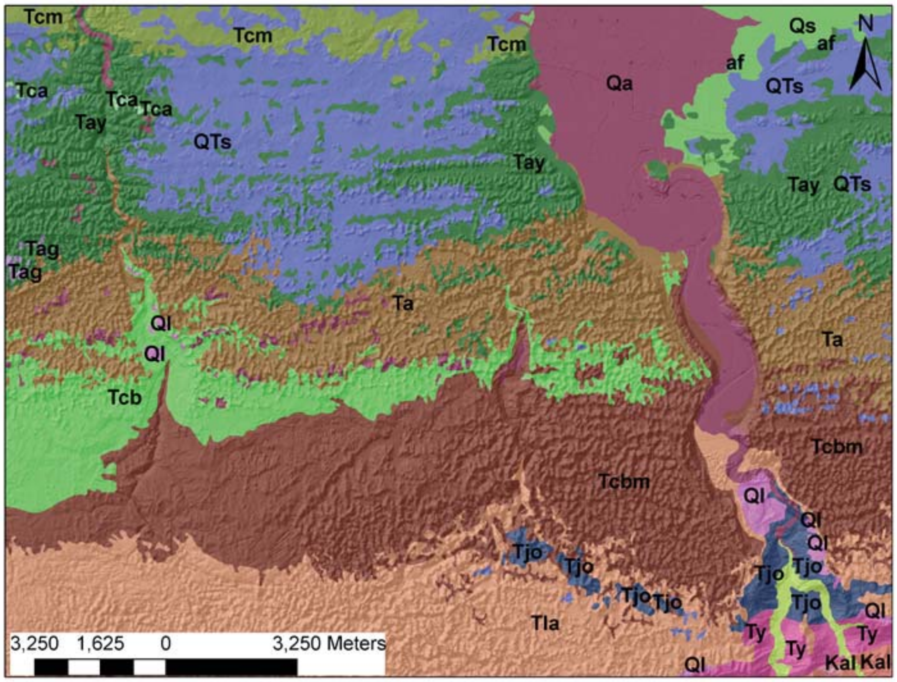

Figure 1.3 Geology of area USGS polygon from (Bawiec 1998) Limestone formations are denoted as: Ta, Tay, Tcb, Tcbm, Tcm,Tla, Ts.

Regional faults have not been mapped for the study area. However, some geomorphic alignments might be attributed to NW faulting on the volcanic bedrock (Giusti 1978; Rodriguez-Martinez 1997; Renken et al. 2002) and might be picked up by RS imagery as segmented lineaments (Hung et al. 2005). Noticeable alignments of valleys and karstic hills have been recognized as being influenced by dissolution along joint patterns. Other proposed reasons are the eastward tilt of the PR platform, Easterly Trade Winds (cementation of eastern side of hills) (Monroe 1966), and past fluvial or drainage patterns (Renken et al. 2002). Moreover, alignment of hills, valleys, sinkholes, and changes in river courses can be explained by regional faulting or fracturing (Rodriguez-Martinez 1997; Renken et al. 2002). Such regional trends are: NE (1°-20° & 70°-90°), NW (10°-30° & 80°-90°) and EW Ward et al. (1991) . In karsts, groundwater flow is mostly constrained to fissures created by dissolution of fractures; faulting or fracturing appear to influence groundwater flow and spring type, which are mostly conduit type (Rodriguez-Martinez 1997; Renken et al. 2002). Also, the general strike of the limestone beds tends to favor groundwater flow parallel to bedding, in addition to the gravitational flow in the down-dip direction. Structural control is the reason for the groundwater divide of the two main rivers in the study area (Rodriguez-Martinez 1997). I propose that the method developed by (Bruning 2008) can be applied in this area by adapting the image processing and considering different digitally processed products. Moreover, geomorphic and hydrologic features can be most likely attributed to influences on lineaments corresponding to regional faulting which are mapped herein.

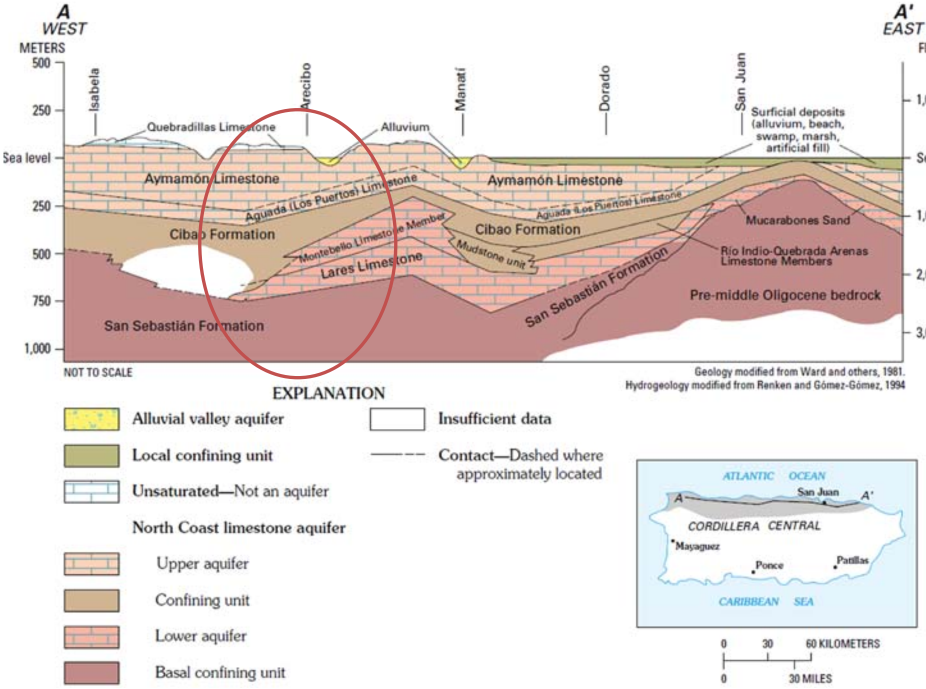

Figure 1.4 General Geology and hydrology of the northern aquifer system, adapted from Renken et al. (2002) . Study area circled in red.

2. Objectives

Because of the lack of applications of remote sensing for characterizing hydrological features of karst systems, this study's objectives were formulated to:

- Adapt and extend previous methods developed by Bruning et al. (2011) to characterize geologic lineaments with an assortment of RS data for a tropical karst terrain.
- Incorporate high-resolution LiDAR DEM in the characterization work.
- Determine if lineaments found using RS imagery correspond to VLF-EM survey data, literature and/or field verification data.

3. Methods

The methodology follows that developed and tested by Bruning (2008) to map lineaments in hard-rock terrain in Nicaragua. In her work, images from different RS sensors of diverse spectral, spatial and temporal resolutions (Quickbird, Landsat ETM+, ASTER and RADARSAT-1), as well as a DEM derived from a topographic map, were chosen and a combination of various digital image processing techniques, such as Intensity Hue Saturation (IHS) Transformation, Principal Component Analysis (PCA), Normalized Vegetation Indices (NDVI), Tasseled Cap (TC) Transformation, and Optimum Index Factor (OIF), were evaluated. Uniquely for RADARSAT-1, dry and wet season images change detection and edge and texture enhancements were completed. Bruning (2008) used 12 products, which did not include Landsat ETM+, that best illustrated previously mapped faults and fracture phenomenology. Lineaments for each of the 12 remaining products were manually extracted and synthesized by means of a coincidence analysis. The coincidence analysis involved 3 essential steps: 1) application of a buffer of adequate extent to account for fracture zone representation and weathering; 2) creation of a raster sum of all the buffered lineament interpretations; and 3) determination of the coincidence level (how many time a lineament interpretation is repeated) cutoff for the created buffer. Those lineaments interpretations with a level of coincide of 4 or more where categorized as "real or existing" lineaments. Finally, to determine the influence of lineaments, pumping tests were carried out in existing wells and they showed that well yield was higher in wells closer to lineaments identified by the coincidence raster. Image performance assessment showed RADARSAT-1 to be the better sensor to enhance true lineaments in this hard-rock setting but that it was not able to identify all the lineaments that were detected in other products and field verification (Bruning et al. 2011).

In this analysis, the previously explained methodology from Bruning (2008) was adapted to the karst terrain. The sensors and processing that were used for this work include: a high-resolution LiDAR DEM, Landsat ETM+ and Landsat TM and digital derived products (Landsat PCA including Thermal band in addition to stand alone interpretation of the Landsat ETM+ thermal band and ASPECT analysis to the LiDAR DEM). In all there was a total out 17 out of 50 products included (Table 3.3) for the coincidence analysis. Existing hydrogeological data, mostly from springs, was used as part of the ground-truth data. Also VLF-EM profiles were carried out to correlate positive electromagnetic anomalies to the existence of lineaments. Geomorphic mapping was also performed.

Since there are only few minor faults and no major faults mapped in the study area, except one east-west trending fault (Renken et al. 2002), a fracture phenomenology assessment was not conducted. However, lineaments mapped in this study were compared to a lineament map created for the area by Ward et al. (1991) in the results chapter. The hydrology and tectonic history is poorly understood in the study area, which suggests that the approach of this study to characterize geologic lineaments could be important for future studies in the area. The following subsections provide more detailed descriptions of the steps followed in this study.

3.1. Remote Sensing Analysis

Remote sensing images were exploited to delineate lineaments that potentially influence shallow groundwater behavior in the Rio Tanamá and Rio de Arecibo basins in the Northern Karst of Puerto Rico. A selection of RS imagery was used in this project as opposed to only a single image. Using more than one sensor with more than one band combination in lineament mapping gives us more information from which to exploit features.

3.1.1.Image Selection and pre-processing

Images were chosen to complement each other in spatial, spectral and temporal resolutions. Data from optical sensors (ASTER, Landsat TM & ETM+; and non-optical sensors: LiDAR and RADARSAT) were used coupled with National Elevation Datasets (NED). ASTER offers visible near infrared imagery of 15-meter resolution. ASTER also includes short-wave infrared (SWIR) and thermal infrared (TIR) bands, but these were not used. The SWIR sensor was damaged and the TIR spatial resolution is coarser (90 m) than Landsat ETM + and TM thermal bands (30 and 60 m, respectively). LiDAR (Light Detection And Ranging) was chosen due to its fine spatial resolution of 2 m and its ability to “see” through vegetation cover. LiDAR is an active remote sensing technique, which means that unlike most optical RS satellites it does not depend on the Sun’s energy to acquire the data because it has its own energy source. Two Landsat images were acquired for dry and wet seasons. The acquisition times of the Landsat images (1989 wet season and 2003 dry season) are far apart because of the lack of cloud-free images for this tropical area. Similar issues were encountered when trying to find a cloud-free ASTER image. ASTER night images for this area were not available and RADARSAT-1 imagery was sparse for the area during the times that the other data were acquired. Optical sensor statistics of each image are reported in Table 3.1.

Table 3.1
Remote Sensing image parameters

Parameter	**RADARSAT-1 SWB**	**RADARSAT-1 ST5**	**ASTER**	**Landsat ETM+**	**Landsat TM**
Acquisition Date	2007-11-20	2008-01-08	2010-02-10	2003-01-22	1989-10-06
Acquisition Time GTM	10:19:31	22:35:30	15:07:53	14:38:56	14:15:48
Off Nadir Look Angle	32.4207°	34.0020	VNIR -.022 TIR 0.004	n/a	n/a
Orbit	Descending	Ascending	n/a	n/a	n/a
Polarization	HH	HH	n/a	n/a	n/a
Look Direction	R	R	n/a	n/a	n/a
Sun Elevation	n/a	n/a	50.4°	41.0°	52.0°
Sun Distance	n/a	n/a		0.984 AU*	
Sun Azimuth	n/a	n/a	143.2°	141.091644°	126.378533°

*1 Astronomical Unit (AU)=149, 598, 000 Km used for conversion to at-sensor reflectance calculations

Image processing was performed with ERDAS Imagine 9.3 (Leica Geosystems Geospatial Imaging, LLC. 2006) and geo-referencing projected to WGS 1984 UTM Zone 19N. Then the image was subset to the study area.

3.1.1.1. ASTER

ASTER (Advanced Spaceborne Thermal Emission and Reflection Radiometer) imagery was chosen primarily for its spectral and spatial resolution. Ultimately the spatial resolution in the visible bands provided the most utility. The ASTER L1B image was acquired from Warehouse Inventory Search Tool (WIST)(Survey 2009) and processed using ERDAS imagine using re-sampling bilinear interpolation method and converted to radiance from Digital Number (DN). The available bands were 1-3 visible and near-infrared (VNIR) with 15-m spatial resolution and 10-12 thermal infrared (TIR) with 90-m spatial resolution because since April 2008 the sensor for bands 4-9 (SWIR) stopped working. Data prior to 04-2008 had high cloud coverage in the area and therefore were not useable for the purposes of this project.

3.1.1.2. LiDAR

For this study, LiDAR data were acquired on December 10, 2004 using a Leica ALS50 Lidar system on a C-GNWC aircraft by the 3001 Spatial Data Company for the U.S. Army Corps of Engineers. The use of LiDAR is unique to this study. Bruning (2008) used a Quickbird image of her study area and it had a 0.6-m resolution, which turned out to be too detailed for lineament identification. The spatial resolution for the LiDAR image was 2 m and provided vastly superior qualities for characterizing the karst features in this study area. Raw LiDAR data and flight information from were acquired from the GIS and Remote Sensing Lab International Institute of Tropical Forestry in Puerto Rico and later filtered using ArcInfo 9.2. Coverage data contained easting, northing and elevation (x,y,z) and raw .LAS files (binary file format created for LiDAR elevation data) with return number (first, second or last). Filtering of the data was done using a multi-scale curvature classification (MCC) algorithm (Evans and Hudak 2007). Points classified as ground returns via the MCC algorithm were used for the generation of the DEM using Inverse Weighted (IDW) interpolation (variable search radius, 12 points). Table 3.2 shows the LiDAR data collection parameters.

Table 3.2
LS50 sensor parameters from (Dixon 2004) and (Leica-Geosystems 2004)

Property	**Value**
Wavelength	1064 nm (NIR)
Airspeed	125 knots
Flying height (above mean terrain)	2895 m
Laser Pulse rate	28400 Hz
Field of View	41°
Area/Point (average)	4.32 m^2
Horizontal accuracy	11-46 cm
Vertical accuracy	13-30 cm
Scan rate	16 Hz
Point Density Average	0.24 pts/m^2
Illuminated Footprint Diameter (@ 1.e^2 energy)	0.915 m

3.1.1.3. NED DEM

The National Elevation Dataset (NED) Digital Elevation Model, a 30-m DEM, was obtained for the study area from the USGS Seamless Data Warehouse (U.S.Geological-Survey 2010).

3.1.1.4. Landsat ETM +

The Landsat ETM+ sensor was chosen due to its potential in geological applications and its spectral resolution and spatial resolution especially for the thermal band. Also, this was the only sensor that had wet- and dry-season images available, although the image acquisitions are 14-yrs apart. Images where downloaded from the U.S. Geological Survey Earth Explorer (U.S.Geological-Survey 2011a).The original images were stacked and subset in ERDAS and histogram correction was made. Two stacks were made: one including bands 1-5 and 7 (without the thermal band) and another including 1-7 (with the thermal band). These two images were used in the PCA.

3.1.1.5. Landsat TM Wet Season

The COSTZ (cosine of solar zenith angle), or COST, model of was used to convert DN vales of the Landsat TM image to reflectance. This model uses the Chavez (1996) atmospheric correction coupled with radiometric correction. Additional information on the steps taken and underlying theory of the model can be found at the Arizona Remote Sensing Center (2004). Parameters needed by the model include: Earth-Sun distance, Sun elevation angle, and minimum DN values. Earth-Sun distance and Sun elevation angle values are for the acquisition time of the image. The distance was acquired by STELARRIUM. The Sun's elevation angle was obtained from the image metadata. Minimum DNs were manually obtained from each individual band's histogram in ERDAS Imagine.

3.1.1.6. RADARSAT-1

RADARSAT-1 model ST5 and SWB imagery, 12.5- and 50-m resolution, respectively, were acquired from the Alaska Satellite Facility (ASF) of the Geophysical Institute at the University of Alaska Fairbanks. Two images were obtained: one from the ascending orbit (12.5-m resolution) and the other from the descending orbit (50 m). The images were orthorectified and geolocated with a USGS National Elevation Dataset (NED) 30-m DEM using ASF's MapReady© Remote Sensing Tool Kit software (2007). An automatic water mask had to by be applied due to the large extent of the original image file in order for the software to process the defined area by the DEM (mask). The image had to be further geo-corrected in ArcMAP.

3.1.1.7. Orthophoto

An orthophoto was acquired from September and October 2004 from Earth Explorer and mosaiced together. This image was not used in the lineament analysis but was used for reference due to its high spatial resolution (1 m).

3.1.2.Digital Image Processing (DIP)

3.1.2.1. Synthesis

Multiple DIP techniques are carried out to subsequently collect various products, from which the best at enhancing features of interest (geo-hydrological and geomorphic lineaments specifically) were kept for further analysis. DIP processes used for this study are listed in Table 3.3. RADARSAT-1 image was despeckled using ERDAS Imagine9.3 to remove brightness in the image. This despeckling procedure is shown in the ERDAS Imagine Radar Tutorial and Bruning et al. (2011) explains it further. The process was repeated until the 3rd iteration was reached. A PCA was performed with ASTER and Landsat ETM+ and TM data in order to optimize the information of the image. Performing a PCA helps the user analyze most of the data by removing noise and autocorrelation between bands. It may be used in many applications, including remote sensing. Statistics of the image and PCA, covariance matrices are reported in Appendix A . Also, Intensity Hue and Saturation (IHS) transformation was done but not used in lineament interpretation. No further processing was done on the ASTER image. Various hillshade analyses were done to the DEMs (2- and 30-m resolutions) using different Sun azimuth angles in ArcMap. This was done because some features will show up better when the Sun illumination azimuth changes.

Slope and aspects maps were created in ArcGIS. The definition ArcGIS gives for an aspect is: "Aspect identifies the down-slope direction of the maximum rate of change in value from each cell to its neighbors". "Aspect can be thought of as the slope direction. The values of the output raster will be the compass direction of the aspect." Essentially it is the azimuth of the dip (maximum slope). For Landsat ETM+, two PCAs were obtained: one including the thermal band and one without. In addition, NDVI and NDMI (both defined below) were calculated for the Landsat ETM+ image. These indices were also calculated for the Landsat TM image but were not analyzed any further. This image was acquired roughly a month after Hurricane Hugo passed over the island, making vegetation and soil patterns not representative of a "normal" storm-free wet season. Furthermore, dry season images alone serve better for hydrologic purposes, assuming that vegetation growth and health is being influenced by groundwater presence.

3.1.2.2. NDVI and NDMI

NDVI and NDMI analyses were done on the Landsat ETM+ dry-season image. Both of these indices were calculated using ERDAS Imagine Model Maker using models from (Center 2004). The NDVI can be applied to monitor changes in vegetation. The NDVI ratio minimizes noise due to Sun illumination and other atmospheric factors. This ratio takes advantage of the vegetation reflectance between these wavelengths. The NIR part of the EM spectrum (band 4) corresponds to reflectance of the vegetation plateau and Red EM radiation (band 3) corresponds to chlorophyll absorption (Jensen 2007). The NDVI was calculated in ERDAS Imagine according to:

$$\mathrm{NDVI}=\frac{\mathrm{NIR\text{-}Red}}{\mathrm{NIR+Red}} \qquad (1)$$

The NDMI Index is similar in configuration to the NDVI and can be used to complement the NDVI (Bo-Cai 1996). NDMI uses the 0.86 and 1.2 channels (bands 4 and 5, respectively) on the spectrum(Gao 1996). Because these two channels are on the vegetation reflectance region and are not widely affected by atmospheric or soil conditions nor is the 1.24 channel very sensitive to liquid water changes, the NDMI is especially useful in densely vegetated areas to determine liquid water changes(Bo-Cai 1996). This index was used in order to determine relative boundaries humid areas in the area.

$$\mathrm{NDMI}=\frac{\mathrm{Band\ 4\text{-}Band\ 5}}{\mathrm{Bamd\ 4+Band\ 5}}\ \text{or}\ \frac{\mathrm{IR\text{-}SWIR}}{\mathrm{IR+SWIR}} \qquad (2)$$

To calculate these indices, the original image was converted to reflectance from the original Digital Numbers (DNs). DN is a measure of radiance acquired by the sensor. Pixel values were converted to satellite reflectance sensor using ERDAS imagine, and the calculated LMAX (maximum spectral radiance as Watts per sr per m^2 and LMIN (minimum spectral radiance) values for each of the visible bands from the image metadata are listed in Appendix B. This was done using Landsat ETM+ Reflectance Conversion Tool on the Spectral Enhancement menu. The parameters the model uses are solar elevation, solar distance, LMAX/LMIN values and solar exothermal irradiance. The values for the Sun elevation of 41.6° was acquired from the metadata and solar distance was acquired using STELLARIUM, a planetarium software that allows you to determine planetary positions for any date and time, and the value was determined to be 0.9841336 AU at 10: 35: 18 on 2003-01-22. Solar exothermal irradiance values are built into the model.

3.1.3.Evaluation of Image Products

A large number of image products were obtained after the DIP work. In order to identify the products best suited for lineament extraction, all products were visually judged on their ability to show linear features and their resolution. All of the products (52) are listed in Table 3.3 and those that were selected as the best are highlighted in grey shading (17 plus two additional interpretations from a 2nd interpreter).

Table 3.3

Products derived of each image. Those highlighted in grey are those ultimately used in the coincidence raster for further analyses

Sensor	**Processing Level**
RADARSAT-1	Stretch enhancement
	Original image
	Despeckle - 1st
	Despeckle - 2nd
	Despeckle - 3rd
	Edge enhancements:
	E Filter
	N Filter
	NE Filter
	NW Filter
	SW Filter
ASTER	VNIR Stretch Enhancement
	Combination of Bands 1,2 &3(+second interpreter)
	VNIR PCA
	VNIR IHS
	Combination of VNIR PCA
	TIR Stretch Enhancement
Landsat ETM+	Original image
	Reflectance Combination of Bands 1-5 and 7
	Thermal Band
	Panchromatic band
	IHS
	NDMI
	NDVI
	PCA visible bands combination
	PCA Visible + Thermal band Combination
	TASSELED CAP
	Hydrothermal indices

Sensor	**Processing level**
Landsat TM	**Reflectance Combination of Bands 1-5 and 7**
	IHS
	NDMI
	NDVI
	PCA visible bands combination
	PCA Visible + Thermal band Combination
	TASSELED CAP
	Hydrothermal indices
Lidar DEM	**Mosaic**
	Hillshade (HS) 90 Azimuth
	HS 135 Azimuth
	HS 180 Azimuth
	HS 225 Azimuth
	HS 275 Azimuth
	HS 315 Azimuth (+ 2nd interpreter)
	Aspect Map (not used in coincidence analysis but used in geomorphotectonic analysis)
	Slope
NED DEM	**Mosaic**
	Hillshade (HS) 90 Azimuth
	HS 135 Azimuth
	HS 180 Azimuth
	HS 225 Azimuth
	HS 275 Azimuth
	HS 315 Azimuth
	Aspect (not used in coincidence analysis but used in geomorphotectonic analysis)

3.1.4.Lineament extraction

A technique similar to the one used by Bruning et al. (2011) was used to manually extract lineaments from the images. A lineament is defined as a linear geologic or vegetation trend/boundary expressed at the surface of the earth. Lineaments were digitized on screen using ArcGIS. Images were analyzed once for local or detailed focus and a second time for more regional lineaments of larger extent. A second interpreter analyzed two images (ASTER images (bands 321) and the LiDAR DEM) in the same manner. Subsequently, each lineament map was analyzed for orientation trends in MATLAB code by Escobar-Wolf (2011) . Density maps were also created in ArcGIS and some are displayed in the Results Section. In order to filter out lineaments that were not repeatable or “false,” a coincidence analysis was done (Bruning et al. 2011).

3.1.5.Coincidence Analysis

In order to filter out “false” or nonexistent lineaments and to determine areas that are prone to contain areas of geotectonic or geomorphologic activity that may influence groundwater flow behavior, the coincidence analysis method (Bruning et al. 2011) was used. A 90-m buffer was used. This buffer was chosen by measuring and averaging the width of 33 lineament features observed in the orthophoto. A total of 19 lineament interpretations were used in the coincidence analysis. Those lineaments considered “coincident” are those that were interpreted 5 or more times (i.e., had a coincidence level of 5) (Bruning et al. 2011). In this study, the chosen coincidence level cut off of was originally 7. This level of coincidence was chosen because there were 8 image product interpretations from the Landsat (ETM+ & TM combined due to their similarities) sensor. Consequently, any lineament interpretation that had a lower coincidence level than 7 was removed from the coincidence raster analysis. However, many features that were present in most of the products were present in the coincidence raster as segments or not represented at all. Therefore, the original level of coincidence cutoff value was too strict and so it was decreased to 5 and a more visually acceptable coincidence raster was obtained. With this change one can still distinguish between the start and end of a lineament. Though using a cutoff values off 5 might be too generous and results in a coincidence raster that is somewhat cluttered. The lower cutoff also risks in lineament detection from only one sensor image, but this is actually a rare occurrence and is discussed in the next section.

3.1.6.Aspect & Elevation

Even after decreasing the coincidence level cutoff, what seemed to be regional features were being shown as separate segments (a common issue when mapping lineaments). In order to “connect” segmented lineaments and to map regional lineaments, the final coincidence raster was overlain on the

LiDAR Aspect analysis and a complementary lineament interpretation was obtained. This map helped me gain a better understanding of the extent of regional fracturing. Furthermore, the Aspect Map showed regional lineaments as a series of continuous slopes facing a similar direction, which can be attributed to faulting (Jordan et al. 2005). In addition, the LiDAR DEM and Aspect analysis were used to map lineaments corresponding to river channel bends to further corroborate the existence of geomorphic features associated to the existence of faults in the area (Della Seta et al. 2004; Jordan et al. 2005).

3.2. Field Evaluation

To have a better understanding of the correspondence of lineaments to hydrology and geology, field and published data were acquired to evaluate the representativeness of the RS interpretations. Previously published field data included a geological map (Bawiec 1998), spring locations (Rodriguez-Martinez 1997), and sinkhole location (Alemán González 2010). Additional field work (geomorphic mapping and geophysics) was performed in this study as outlined below.

The general objective of the field evaluation in this study is to determine the correspondence of lineaments from the coincidence raster and aspect analysis to features found on and below the ground. A field campaign to Puerto Rico was carried out from 10-20 May 2011. Annually this time corresponds to the end of the "dry" season for this area. The "dry" season in Puerto Rico is not completely without rain, it is just the season where rains are less in amount, duration, and frequency. During these field campaign geomorphic features indicating faulting and fracturing mapped. Also VLF-EM profiles were run mostly perpendicular to main features identified in the lineament analysis.

3.2.1. Geomorphic Mapping

Once in the field, morphological features ,which are topographic expressions of faults and fractures, which include, joints, fractures, saddles, scarps, river channel bends and slope breaks among others (Della Seta et al. 2004; Jordan et al. 2005), were mapped . Positions of field-observed features and their orientation were saved on a Garmin GPSMAP 60CSx along with digital photographs of the outcrop. These features were then compared to the coincidence raster and aspect interpreted lineaments.

3.2.2. VLF-EM Geophysics

Very Low Frequency—Electromagnetic (VLF-EM) surveys were conducted using an (ABEM 1989) (Sundbyberg, Sweden) WADI VLF receiver. The WADI was operated by one person, which allows for survey transects wherever one can walk. The WADI is a backpack portable instrument that measures, in this case using a 21.3 Hz frequency, at stations every 10 m across a survey line. The process was repeated for 24 VLF survey lines oriented approximately S-N, because most lineaments trend W-E. Survey lines were made as closely to orthogonal to the features of interest as possible. Making perpendicular transects allows for stronger currents and therefore a better representation of the anomalies' character (depth, dip, extent).

The WADI (VLF-EM receiver) detects eddy currents created by low-resistivity bodies in the subsurface as a result of inductance from a primary field from radio transmitters operating at 15-30 kHz. Such bodies can include, but are not limited to, linear and steeply dipping water-filled fractures (ABEM 1989), faults, iron ores, pipelines, salt water and other high conductivity bodies. This secondary magnetic field (90 degrees in phase with the primary field), created by the eddy currents, is separated into two components and measured by the instrument: in phase (real) and out of phase (quadrature or imaginary) with the transmitted field. These two components are plotted together and whenever there is conductive body in the surface, it will show as a "cross-over" (i.e., zero-crossing points) in the example plotted as Figure 3.1.

Qualitative analysis was done by interpreting filtered VLF-EM data in order to differentiate different fractures/anomalies that could be present in one traverse. Fraser filtering improved the signal of conductive structures by transforming the zero-crossing points into peaks (Monteiro-Santos et al. 2006). Where there is a cross over on the plot, the Fraser filter will show a high positive peak "response" perpendicular to the conductive body. The VLF-EM Data Presentation and Processing Package **IXVLF v 1.04** (Interpex 2010) was used to Fraser filter the data and export it into ArcGIS, where it was overlain over the coincidence raster and Aspect map lineaments.

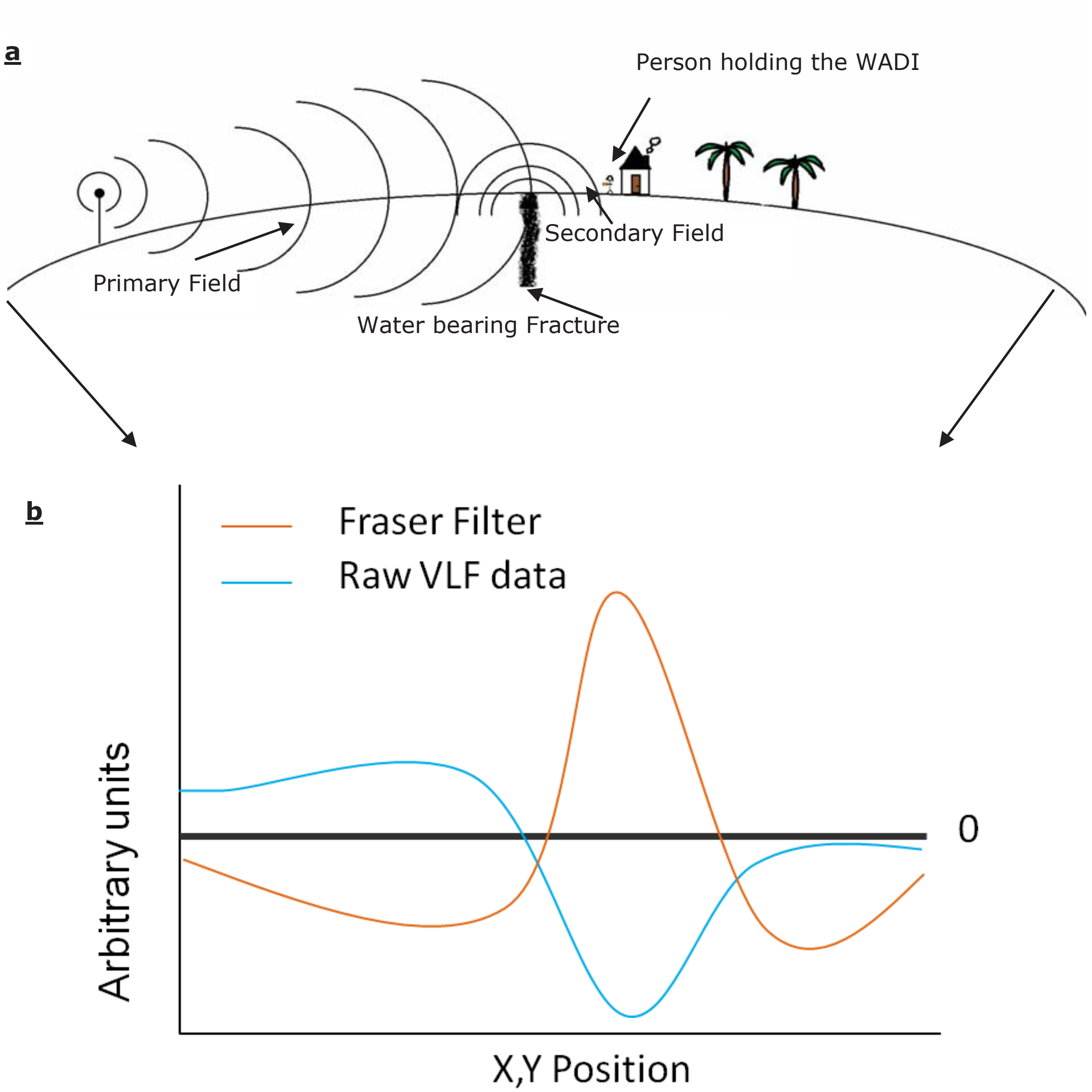

Figure 3.1 a) Diagram showing the behavior of the primary and secondary fields produced by a naval base and the conductive body respectively b) Zero- crossing points of VLF in-phase components of the secondary magnetic field plot showing positive Fraser filter anomaly indicating possible location of conductive feature.

4. Results and Discussions

As outlined above, images from the various sensors listed in Table 3.1 and Table 3.2and elevation data from LiDAR and NED were processed according to Table 3.3, and 17 final products were each individually interpreted for delineating lineaments. The most selected products (6) were derived from the Landsat ETM+ image. Select images and interpretations are presented below. Images and products which were used but not presented below are provided in Appendix C.

The interpreted products were combined into a single coincidence raster by adapting the approach developed by Bruning et al. (2011). The coincidence raster was interpreted to yield the complete lineament map for this work, which is compared to a previously published (Ward et al. 1991) lineament map for an overlapping area. The lineament directions were analyzed using frequency analyses. Lineaments were also compared to the locations of previously and newly mapped springs, previously mapped sinkholes, newly mapped geomorphic features, and interpretations of Fraser-filtered VLF-EM survey data.

4.1. Lineament Analyses

Figure 4.1a shows the original RADARSAT image as noted in Table 3.1. Figure 4.1b shows the images after the 3rd despeckling iteration. Figure 4.1b was interpreted to develop the lineament map shown in Figure 4.1c, which represents one image product. Furthermore, a 45-m buffer was applied on all sides of each lineament creating polygons. As noted above, this buffer was chosen by measuring and averaging the width of 33 lineament features observed in an orthophoto. The polygons were then converted to raster files. Every pixel within this buffered area was assigned a value of 1 and all pixels outside the buffer were assigned zero values, yielding, for example, Figure 4.1 d.

The ASTER VNIR original image shown in Figure 4.2a was used for manual lineament extraction and the interpreted lineaments are shown in Figure 4.2c. This interpretation is an example of the advantages of high spatial resolution for detailed lineament mapping even when there is some cloud cover. Areas covered by clouds can be analyzed in other products. This goes to show that using different image products of different sensors is so important in this type of cloud covered setting. Figure 4.2b is the LiDAR DEM hillshade and it shows that some features that may be indistinguishable in optical imagery are prominent in high-resolution topography data. The lineament interpretation from the LiDAR DEM hillshade shown in Figure 4.2b is shown in Figure 4.2d as an example of detailed and regional interpretation of an image.

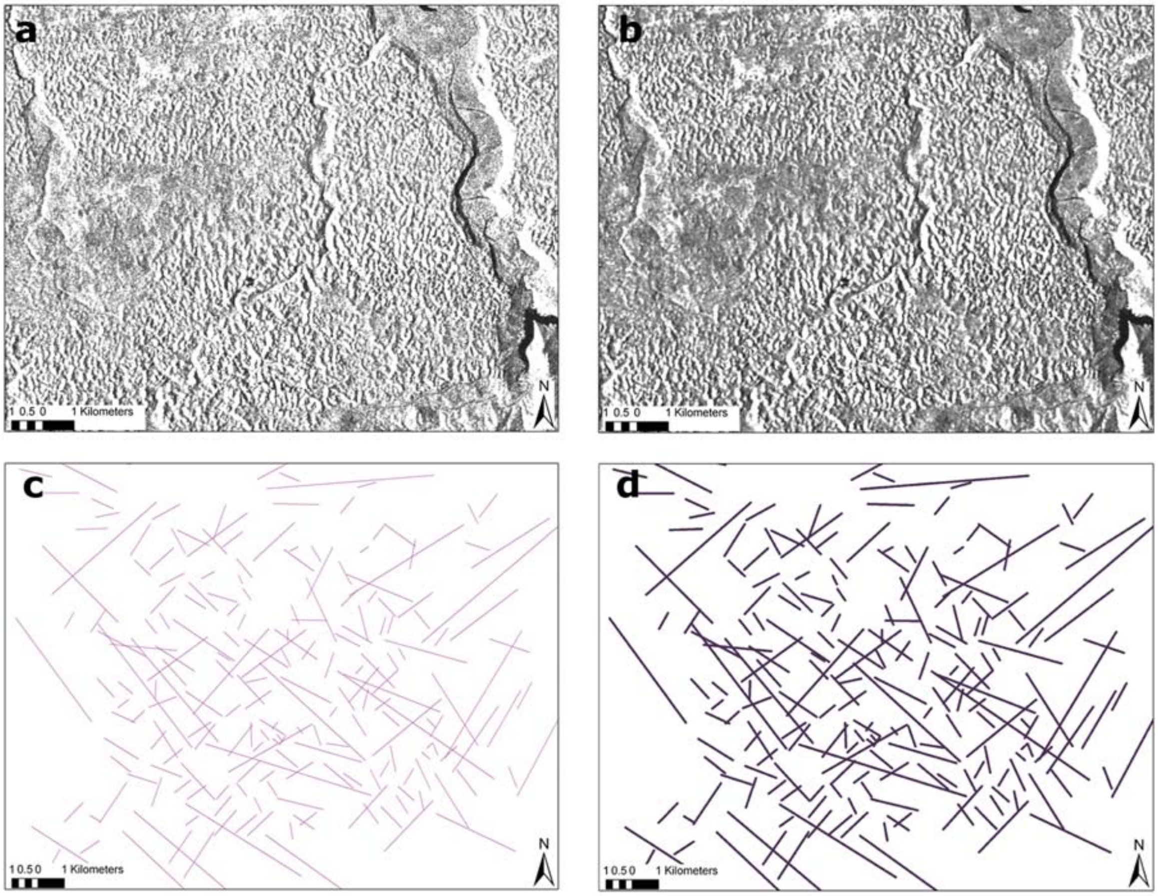

Figure 4.1 a)RADARSAT-1 original image; b) RADARSAT-1 after 3rd despeckling iteration; c) RADARSAT-1 derived lineaments; and d) RADARSAT-1 binary raster format lineaments

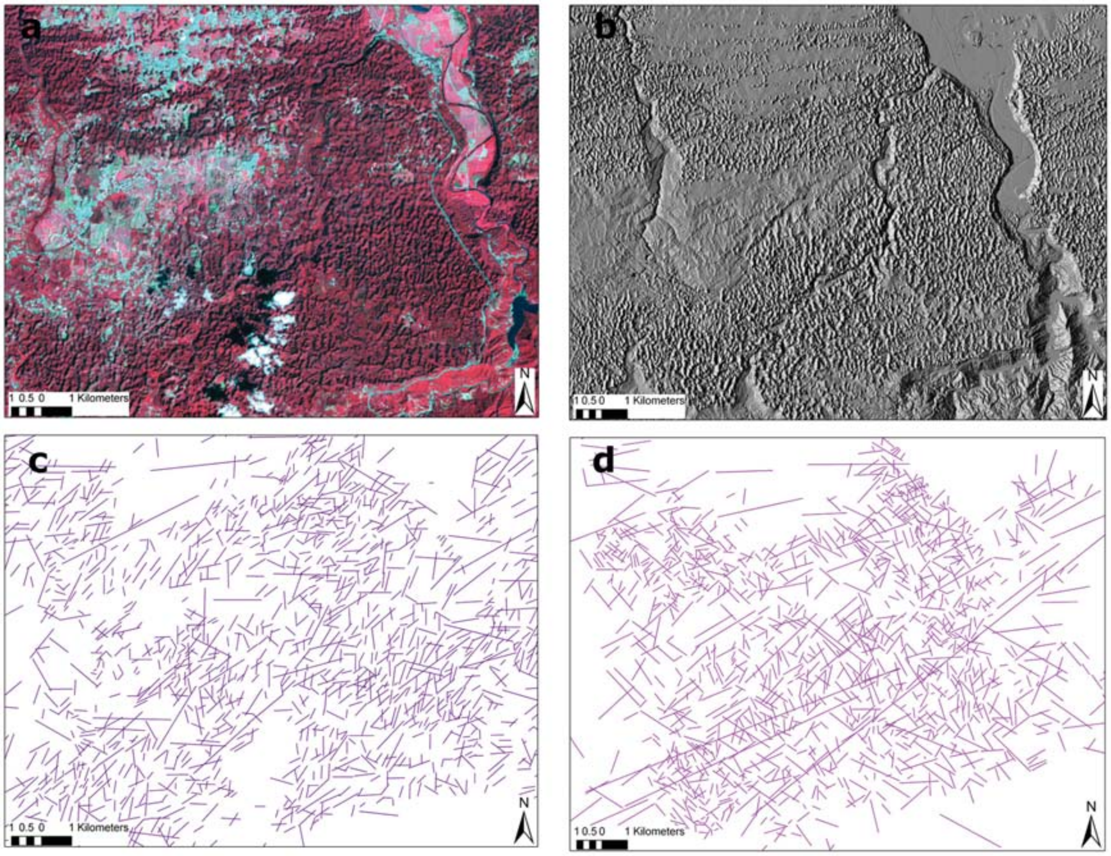

Figure 4.2 a) ASTER original VNIR bands. b) LiDAR DEM Hillshade. c) ASTER VNIR lineament interpretation. d) LiDAR lineament interpretations.

Each of the images listed in grey in Table 3.3 were processed, interpreted, and analyzed in an analogous manner to the two examples provided above. After all lineaments interpretations (19 total) were converted to raster format, they were added in ERDAS (Leica Geosystems Geospatial Imaging 2006) creating a coincidence raster. Those values that only have 4 or less overlapping instances were eliminated from the coincidence raster (Figure 4.3). A unique aspect of this work is the Aspect Map determined from the DEM derived from the LiDAR data (Figure 4.4). Though this product was not part of the coincidence raster construction, for this highly vegetated terrain, this image product turned out to be a very important one in delineating lineaments. Remaining interpreted products are provided in Appendix C.

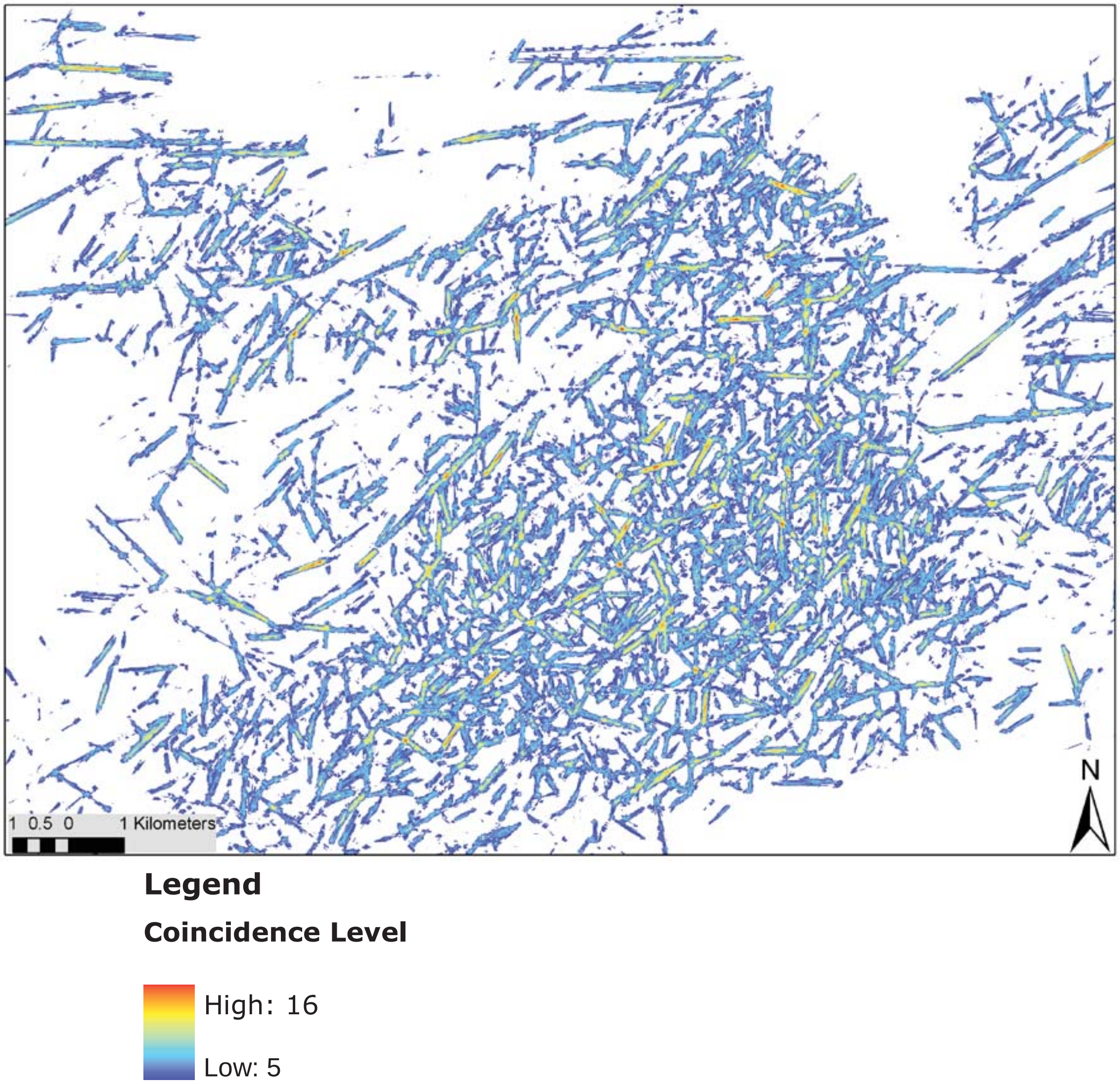

Figure 4.3 Coincidence raster only showing areas were 5 or more lineament interpretations overlapped in the raster summation

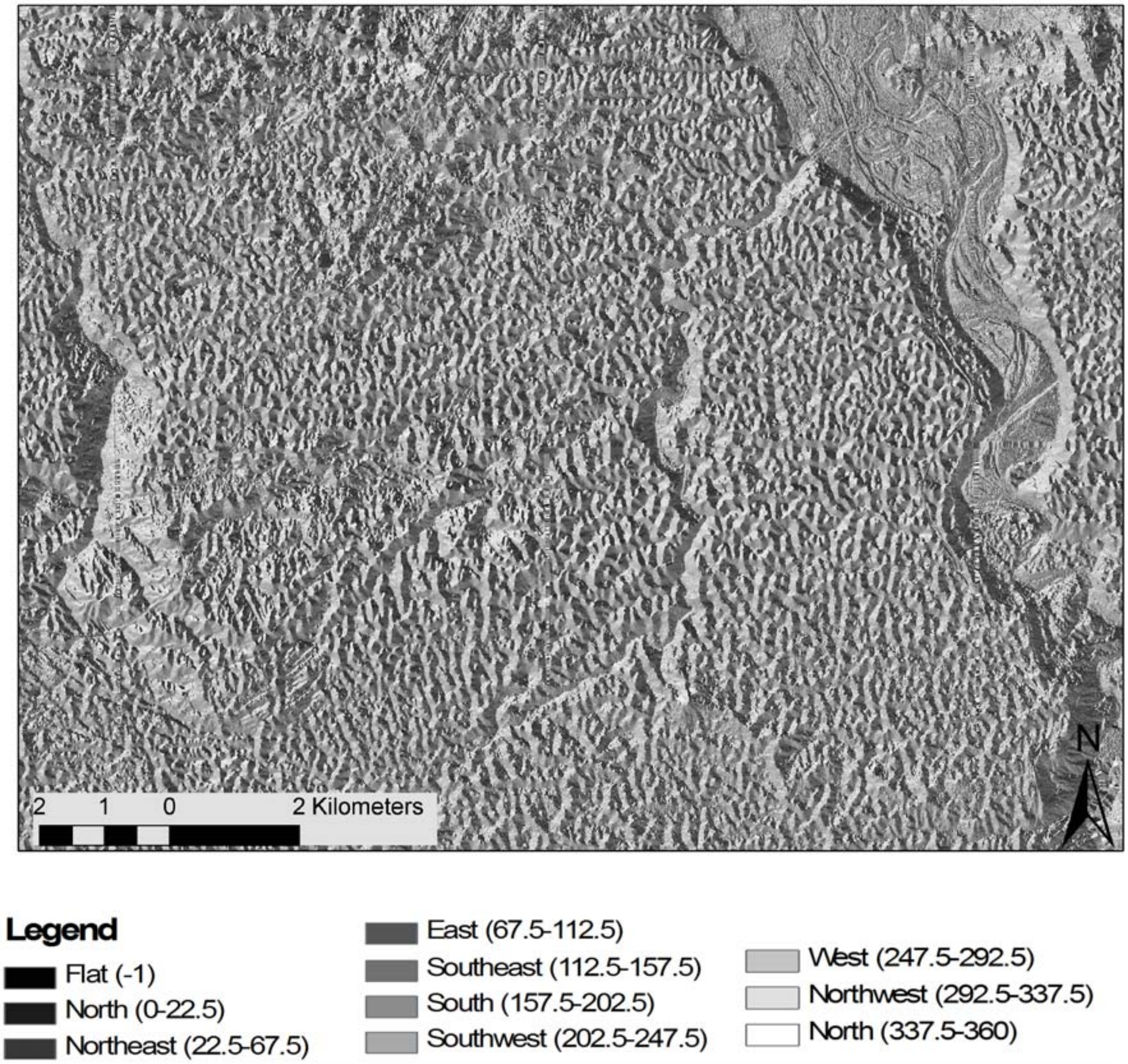

Figure 4.4 Aspect map

Lineaments from the coincidence raster and aspect analysis were digitized manually in order to calculate directional and length statistics, schematically displayed in Rose diagrams (Figure 4.5 and Figure 4.6), and achieve a better description of the map. An orientation analysis was performed and is depicted as a "Rose" diagram in Figure 4.5 and Figure 4.6. The frequency is weighted by the total sum of lineament length in a given orientation, and the scale of the concentric circles is in number-meters.

There is an overall dense presence of lineaments present in the area. Most lineaments follow alignment of hills, river channels and valleys. Larger lineaments are apparent in the NE-SW, N-S, and E-W with minor trends in the NW-SE (Figure 4.5). A summary of the statistics is as following: the number of resulting lineaments is 1536, the maximum recorded length is

4570 m, the minimum length is 103 m, the mean length is 574 m, and the standard deviation is 415 m.

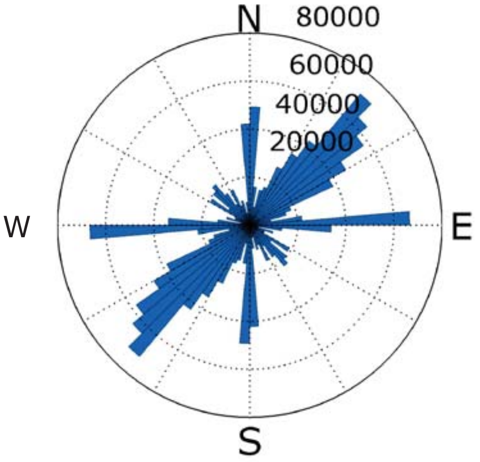

Figure 4.5 Coincidence Analysis Rose diagram. The scale is frequency (number) sum of lineament length (n=5).

There are 193 lineaments derived from solely the aspect analysis shown in Figure 4.4 and its Rose diagram shown in Figure 4.6. From which the minimum length is about 10 m, the maximum is over 4,400 m, and mean is approximately 1300 m (standard deviation about the mean is 800 m). The most pronounced direction for the greatest number and longest lineaments are E-W and the next most common are almost SW-NE.

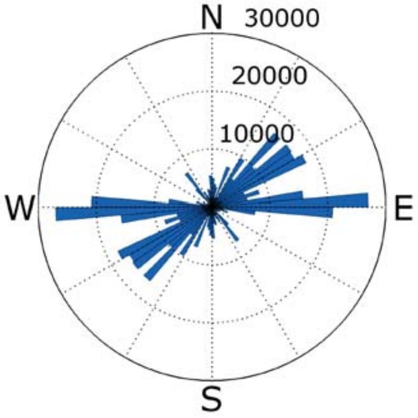

Figure 4.6 Aspect Lineament Rose Diagram

It is also important to note that directional trends of larger NE-SW trending lineaments can be followed along sharp bends along the rivers that are shown on the LiDAR DEM hillshade (Figure 4.7). The mapped lineaments seem to correlate with nearly perpendicular intersections of W-E with N-S and those oriented NW-SE with NE-SW trending slope faces. These lineaments can be observed locally in the river bends and can be followed in the continuing topography (Figure 4.7).

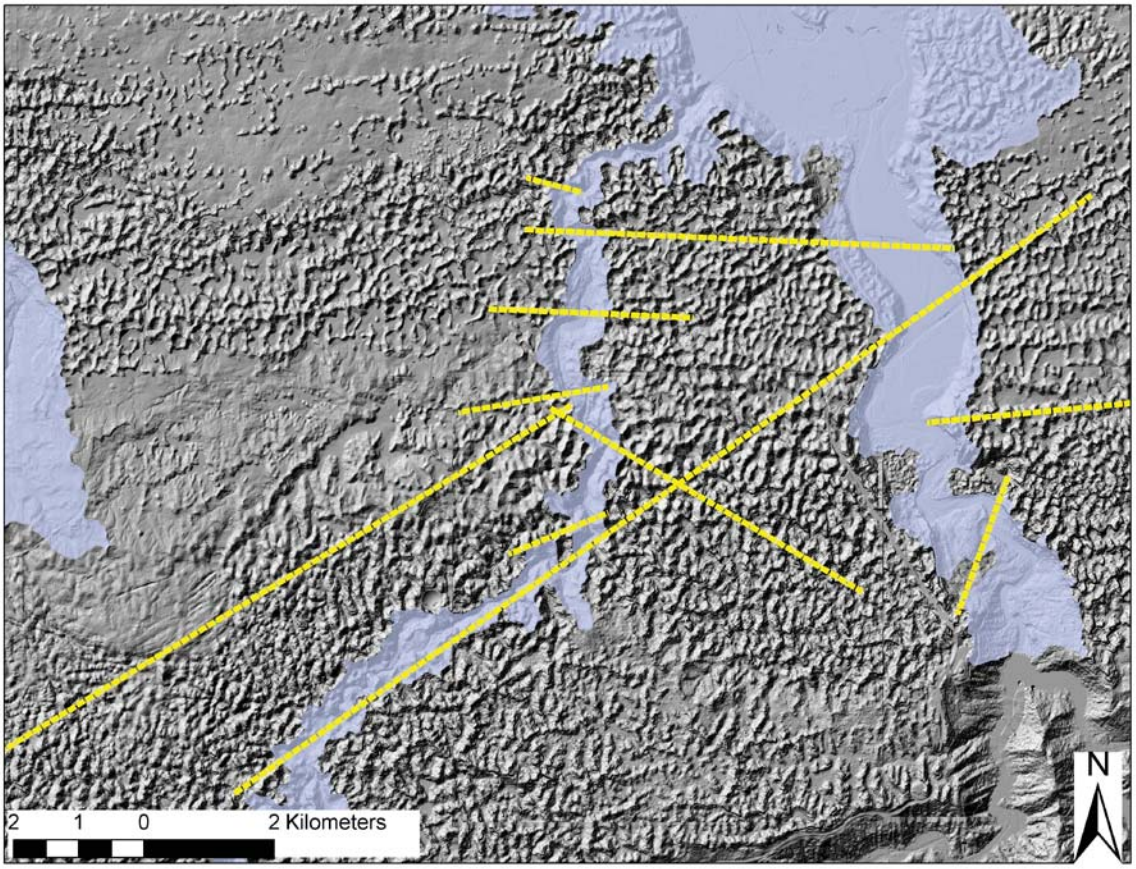

Figure 4.7 River channel bends of near 90° can be attributed to regionally frequent lineaments. Lineaments (orange dashed lines) were interpreted from the LiDAR Hillshade. Areas in blue are the river course and associated floodplains polygon from a USDA Geospatial Data Gateway called the Watershed Boundary Dataset (WBD) (U.S.Geological-Survey 2011b)

Ward et al. (1991) interpreted lineaments that can be correlated to the river bends, geological contacts and ridgelines and theirs are shown as yellow lines in Figure 4.8. The mapping techniques they used seem to miss many lineaments. Even though this study's interpretations may have also missed some regional lineaments, it shows a more accurate representation of lineaments present in the area. One of the advantages of the technique used in this study enables us to detect lineaments from a number of imagery and product. In contrast, they only used one source for interpreting lineaments (geologic map). Figure 4.9 shows the Ward et al. (1991) interpretation that overlapped part of this study area with the interpretations from the coincidence raster. However, the general prevalent directions can be observed in both their study (Figure 4.10) and in this work (Figure 4.5).

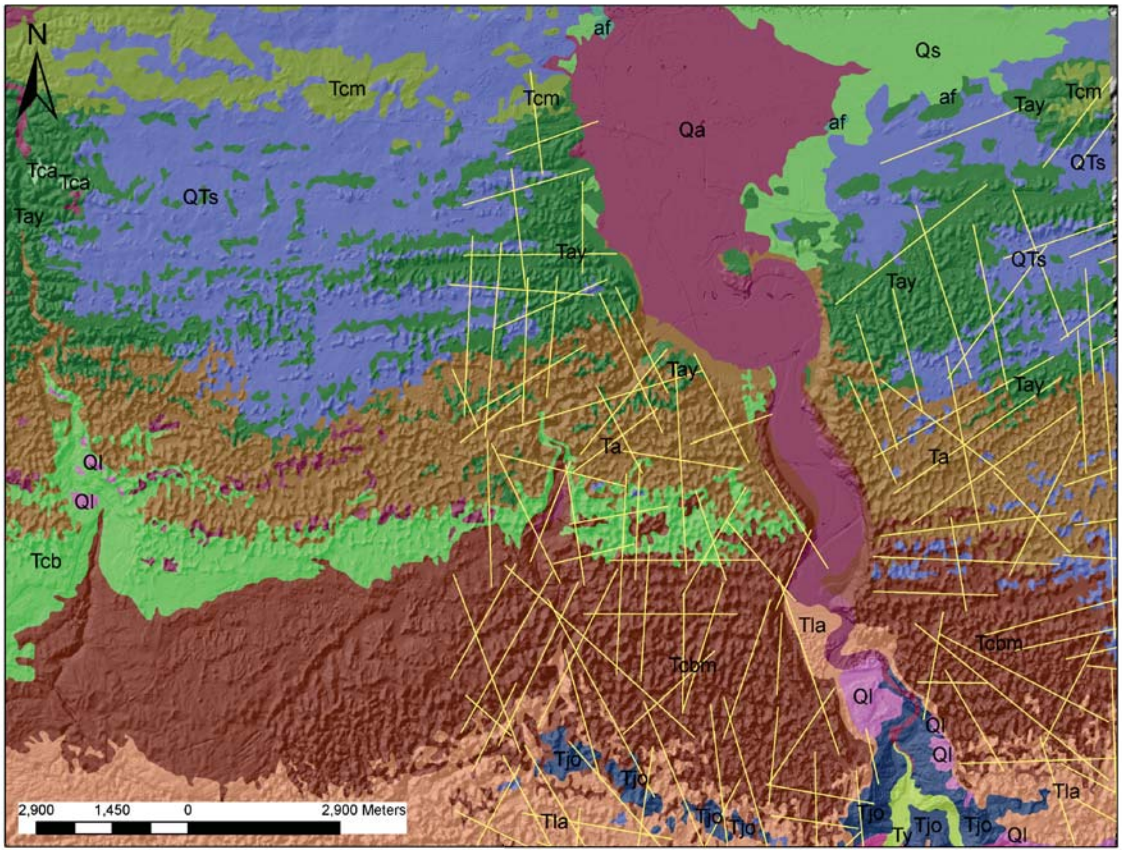

Legend

━ Lineament from Ward et al. 1991

Figure 4.8 Lineaments mapped by Ward et al. (1991) on USGS geologic map polygon from Bawiec (1998)

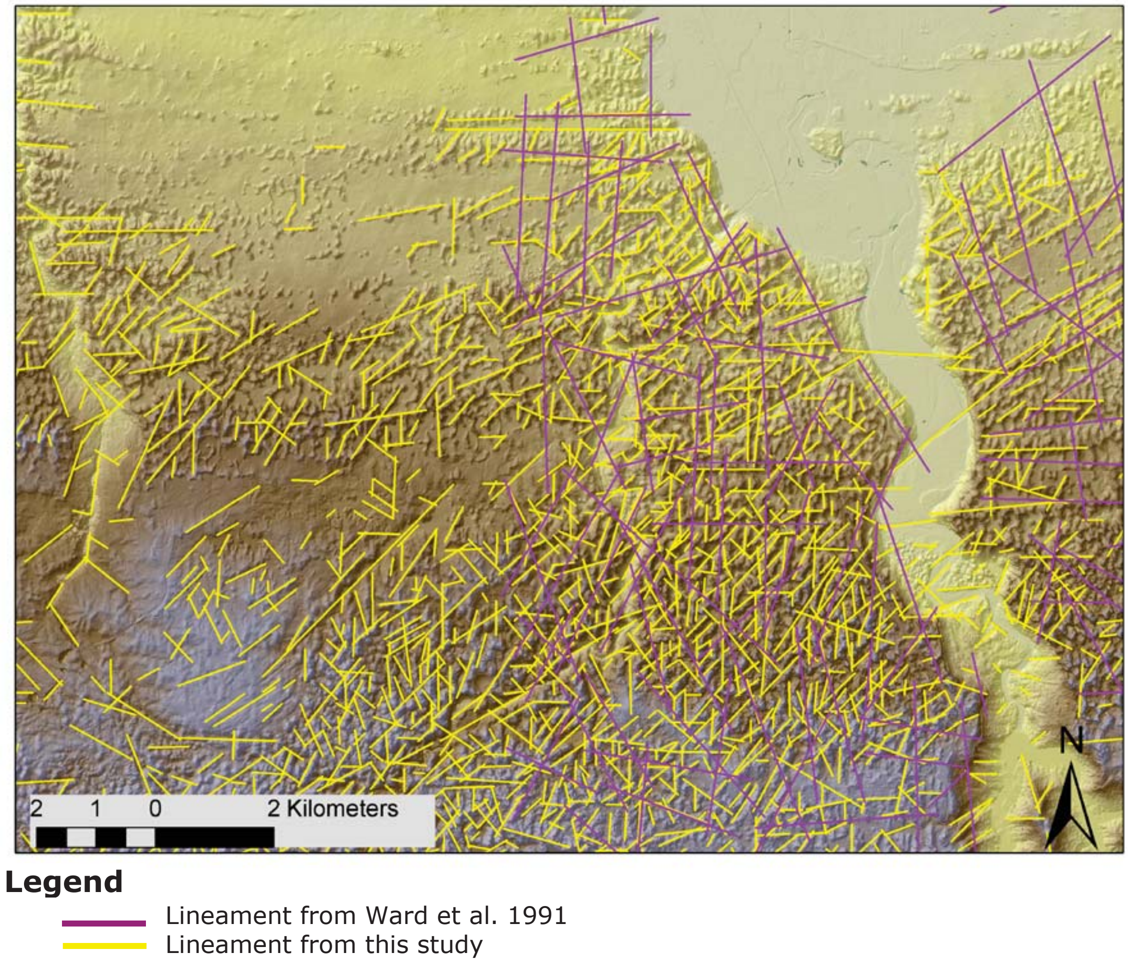

Figure 4.9 Lineaments from Ward et al. (1991) (magenta) and this study's coincidence analysis lineaments comparison (yellow).

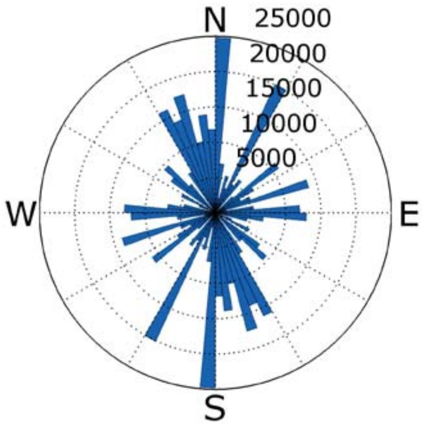

Figure 4.10 Rose diagram of lineaments data from Ward et al. (1991) mapped on geologic map by Monroe (1980).

4.2. Image Performance Assessment

Determining how well the lineaments were interpreted by each image product was done using the Bruning et al. (2011) two-part approach. First, using the coincidence raster (Figure 4.3) and each original lineament interpretations buffered area (e.g., Figure 4.1d). The author determined the fraction of the area of the original lineament that was "false" (i.e., did not lie within the coincidence raster, noted as "% False- identification"), and secondly, the "% of coincidence" between the coincidence raster and an original lineament buffer polygons.

In this study, the image with the highest rank for the "% False-identification" assessment was the PCA of the Landsat ETM+ of which 30.8% of the original interpretation was "false", secondly the LiDAR Hillshade analysis had 32.3% false, and thirdly the PCA of the ASTER VNIR bands with 32.7 % false. Bruning et al. (2011) found this approach was subject to a bias towards a lower quantity of lineaments and longer lineaments. In this study those ranked with lowest false-identification values belonged to those lineament interpretations with average number of lineaments.

As stated by Bruning et al. (2011), the "% of Coincidence" part of the image assessments is biased toward overly interpreted products. This also proves to be true in this study. The Landsat TM (wet season) PCA map shows detailed lineaments making it rank 1st with 63% of the original lineament interpreted on the coincidence raster. This image was acquired roughly a month after a Hurricane Hugo hit the island in 1989. Nevertheless, when compared to the Landsat ETM+ image, similar linear features' trends are observed. In addition, Landsat TM PCA is a compilation of most of the information in Landsat TM bands 1-5, 7, and the thermal band 6 conveniently collected in 3 "bands" PCA 1, PCA 2 and PCA 3. Therefore, regardless if the product spatial resolution (30 m) is not the finest of the group; it has enough information to be able to show detail. The more detail an image shows, the more lineaments can be extracted from it. This means that the total original area is larger and consequently there is a higher percentage of more of it being retained in the coincidence raster, especially if smaller lineaments merge with other lineaments that may not pertain to the same feature on the image (Bruning et al. 2011).

Figures 4.11a & c illustrates Landsat TM PCA and interpreted lineaments, respectively. This interpretation, which had the highest coincidence, shows a high degree of detail and number of lineaments mapped. Consequently, lineaments from Landsat ETM+ PCA (Figure 4.11b) are shown in Figure 4.11d and show fewer lineaments and with a small degree of regional interpretation.

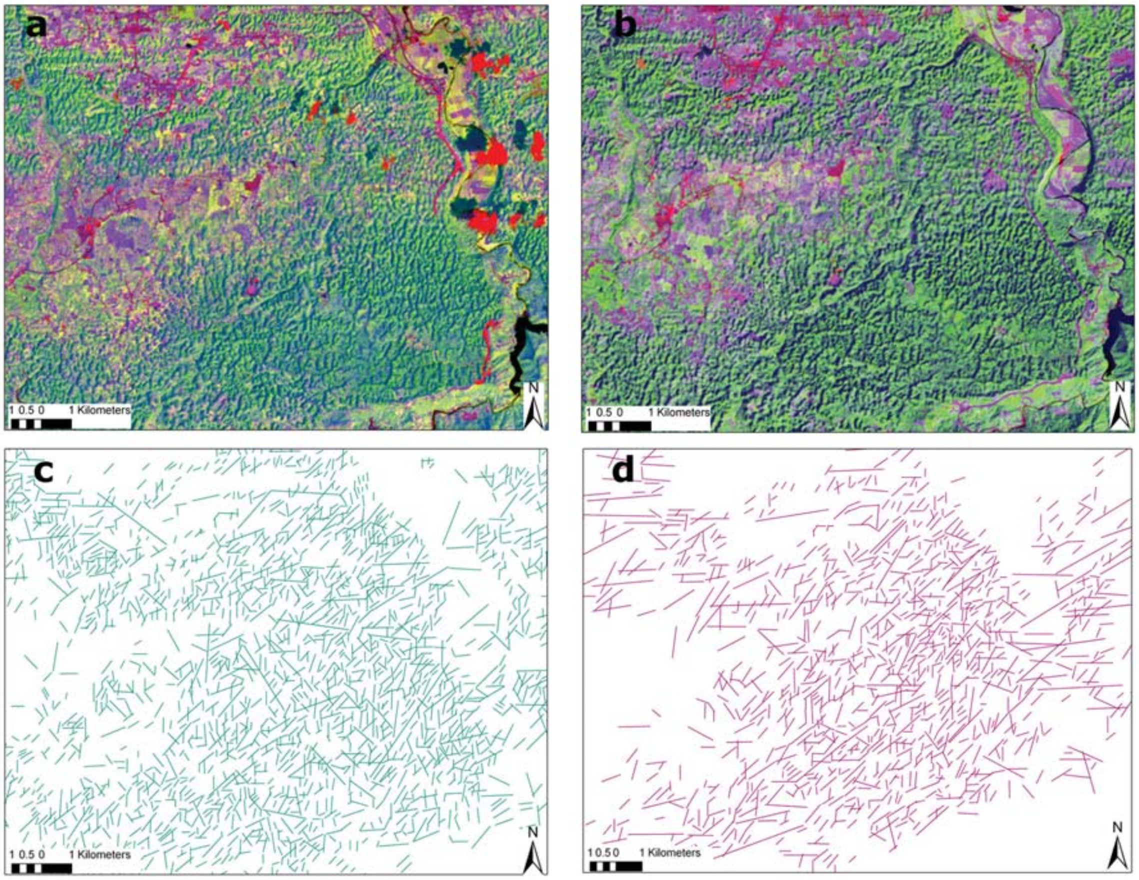

Figure 4.11 a) Landsat TM image PCA b) Landsat ETM+ PCA. c) Landsat TM PCA lineaments d) Landsat ETM+ PCA lineaments.

The second most coincident lineament interpretation in the coincidence raster is the Landsat ETM+ panchromatic band with 60.4 % coincidence. This image includes the spectral resolution of Landsat ETM+ bands 2, 3, and 4 with spatial resolution of 15 m, similar to the ASTER VNIR spatial resolution, which had the 3rd place ranking with 58.3 % and making detailed lineament mapping possible. Combining both assessments this way reduces the biases inherent in each assessment(Bruning et al. 2011). Results of both assessments combined, shown in Table 4.1, show that interpretations from the Landsat TM & ASTER PCA, LiDAR Hillshade analysis and Landsat ETM + panchromatic band, make a thorough analysis of the lineaments in the area. All of the optical images that were used had a solar azimuth of around 140° to 126° at the time of acquisition. This orientation suppresses NW-SE features (Bruning 2008). This may be a reason that NW-SE trending features are not so evident in Figure 4.5 compared to the predominance of NE-SW trends. However, when compared to Figure 4.6, lineaments originating from the Aspect Map, which is a product of the LiDAR DEM, the NE-SW trends are more apparent. Moreover, Ward et al. (1991) found that lineaments in the major units on a geological map mostly trend NW-SE, N-S, and NE/SW, as seen in Figure 4.9 and Figure 4.10. Rinker (1974) found that lineaments in a smaller area on the Northeastern part of this study area also have trends NE-SW and strong but less prominent NW-SE trends.

The influence of the solar azimuth can be counteracted with the use of radar. LiDAR is an active remote sensing technique and therefore it uses its own energy source to gather data. Radar could potentially serve this purpose, but in this study only the ascending orbit of RADARSAT is used because the descending orbit image was of much coarser spatial resolution (50 m) than the ascending orbit (12.5 m). In addition, RADARSAT-1 imagery for this area contains too much distortion due to rapid topographic changes in tropical karst topography.

Before choosing which solar azimuth for the hillshade, all possible azimuths were visually inspected. Azimuths of 275° and 315° highlighted the most linear features. The other azimuths created an "inverted" effect in which lower topographic areas like rivers and valleys seem higher than hills.

Table 4.1
Product Rankings for this Work.

Sensor	Product	Coincidence %	False-identification %
Landsat TM Bands	PCA w/thermal	63	42.1
Landsat ETM + Bands	743	53.8	35.5
	724	50.6	38
	Panchromatic	60.4	47.7
ASTER Bands	PCA	50	30.8
	NDVI	32.6	48
	NDMI	26.5	57.7
	thermal band	18.5	36.4
	VNIR	58.3	45.9
	VNIR PCA 231	42.6	32.7
	Interpreter 2 VNIR	5.3	41.8
LiDAR	Hillshade 275	50.3	32.3
	Hillshade 315	37.4	43.4
	DEM	34.7	44.3
	Interpreter 2 DEM	8.3	42.6
NED	Hillshade 315	41.9	52.1
	Hillshade 275	37.8	49.2
	DEM	44.1	52.8
RADARSAT	Despeckled #3	17.4	54.4

+ False- identification represents the area of the original polygon that is not retained by the coincidence raster. Calculated using original polygon area and retained polygon area.
*% Coincidence is referred to what percentage of similarity the lineaments interpretation has coincidence raster. Calculated dividing retained area by coincidence raster area.
-Areas highlighted in grey are those better ranked in both assessments (higher coincidence percent and less False-identification %.

Because vegetation reflects in the NIR, linear features may also be suggested by vegetation changes and not only geological structure. ASTER VNIR bands are well suited for detecting vegetation reflectance and the 15-m spatial resolution serves in detecting texture patterns and changes. Most importantly, the spatial resolution helps the interpreter distinguish between anthropogenic and geo-hydrological features.

Landsat ETM+ includes a higher resolution thermal band (60 m or 30 m re-sampled) than ASTER (90 m). Mid infrared (MIR) (Landsat bands 5 and 7, ASTER bands 4-9) bands were not available for the ASTER scene used here, hence the Landsat ETM + & TM sensors were included. Bands 5 and 7 have shown to be useful to discriminate between water and soil, due to strong absorption by water of those wavelengths (Jensen 2007). In this study area, there are well defined changes in topography, land use, geology and vegetation. Tropical karst topography is characterized by abrupt changes in topography and aspect, causing changes in vegetation type and health. Making the use of various types of Remote sensing imagery for detecting changes in these features can be helpful when trying to understand groundwater recharge and discharge zones in this type of terrain.

4.3. Field Data

Ground truthing remotely sensed lineaments is complicated, especially in karst topography due to limited accessibility. The approach used in this study was to pinpoint exposures of features that may be associated with the larger lineaments identified in the remote sensing products. In addition, VLF-EM surveys were conducted to investigate lineaments not necessarily expressed at the surface. Not all lineaments interpreted in the remote sensing products exhibited surface exposures (springs, outcrops, hill alignments, sinkholes, etc.), nor was it possible (or practical) to conduct geophysical surveys across all of the interpreted lineaments. Locations of the field work were affected by accessibility and time. Field visited areas (zones) are shown in Figure 4.12.

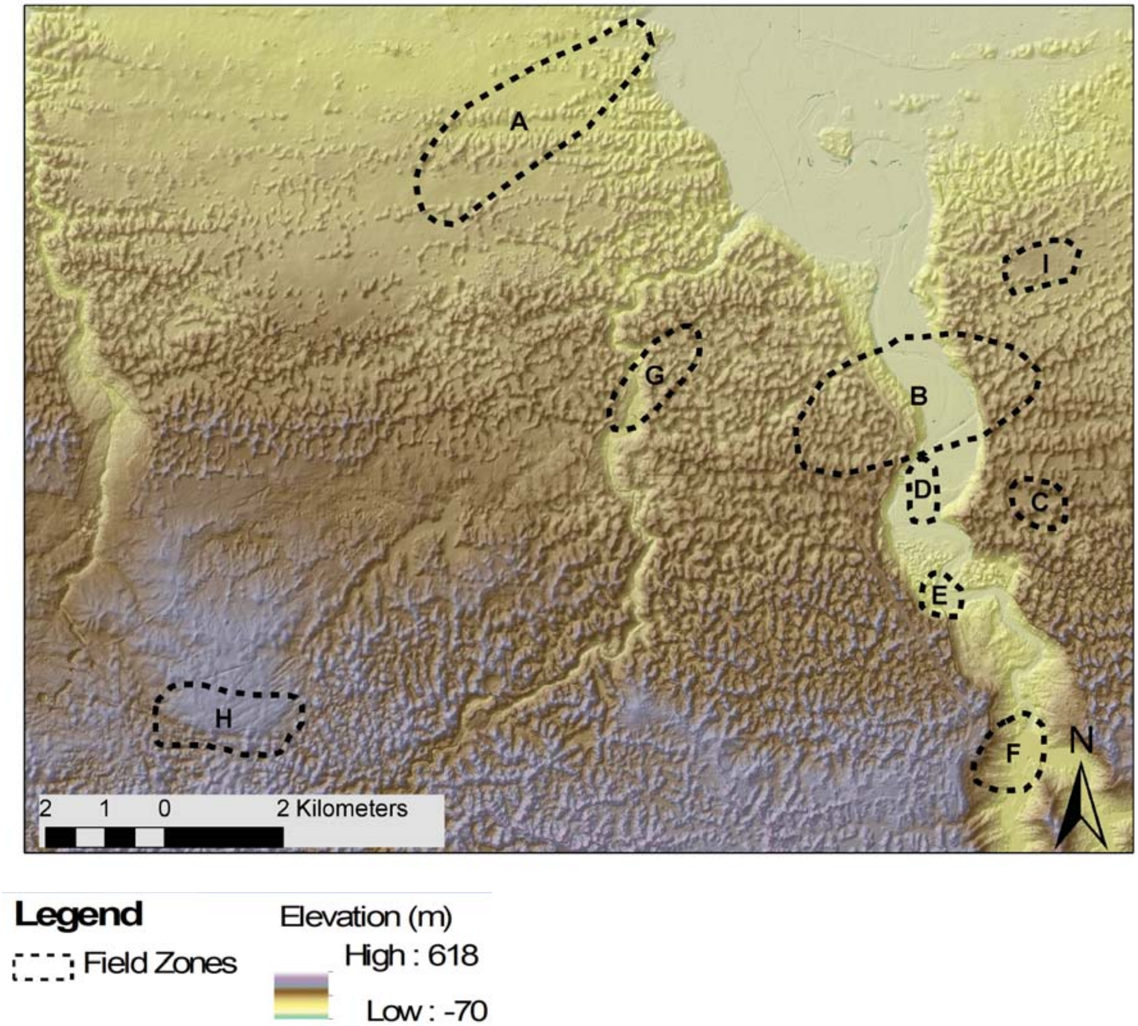

Figure 4.12 General visited areas were located within dashed lines

4.3.1. Geophysics

VLF-EM surveys (Figure 4.13) were made south to north as close to perpendicular as possible to lineaments shown in Figure 4.3 and Figure 4.4. “Fraser peaks” (as defined in Section 3.2.2) correspond to buried conductive bodies, potentially for this site, to depths of approximately 40 m (NGA 2000). The filtered data, as described in Section 3.2.2., can be plotted of the Fraser Filter Value (FFV) corresponding to measurement points along the survey line. For example, Figure 4.14a shows the FFVs for two survey lines. The cooler colors are more negative and the warmer more positive. Conductive anomalies typically appear as positive FFVs. The lateral extents of these surveys are constrained by the landscape and accessibility. If the vegetation was too thick or the land too steep or if it was fenced, then the survey would cease.

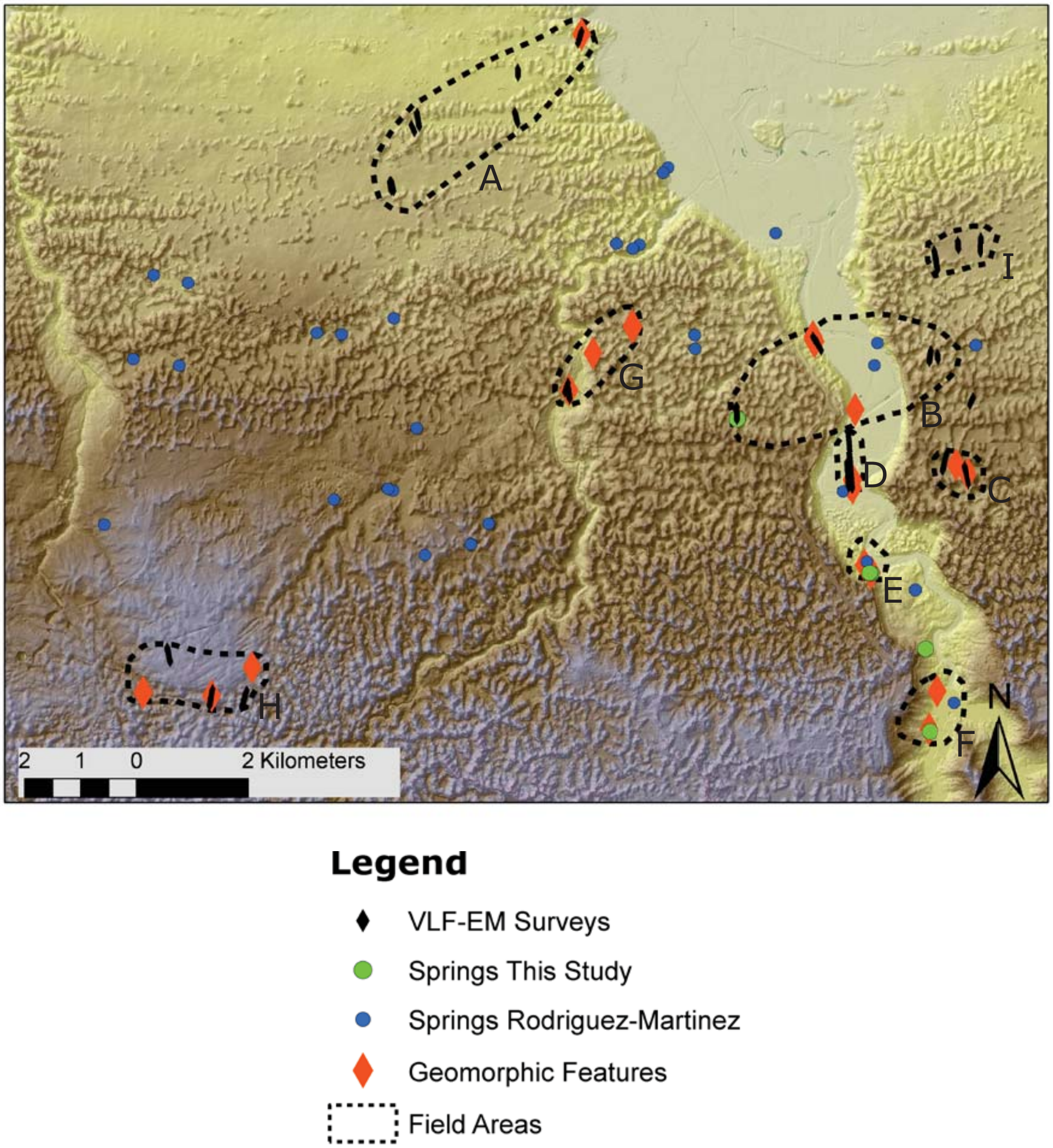

Figure 4.13 Digital elevation mode of the area showing locations of VLF-EM surveys, Springs data from Rodriguez-Martinez (1997)and those found in this studies field expedition and geomorphic features found on site

Conductive anomalies in Zone A, shown as Fraser Filter Anomalies (FFA) in Figure 4.14a, are possibly related to differential erosion across fracture lineaments and may be zones of preferential flow along present joints or fractures (Renken et al. 2002). Figure 4.14 shows that conductive bodies either intersect or are located near the W-E and NE-SW trending coincidence raster features. Conductive anomalies that lie on the quaternary deposits (flat topography) show negative FFVs in contrast to those closer to the karst topography. Negative anomalies may correspond to moderately resistive bodies, i.e., less conductive materials (Al-Tarazi et al. 2008). In Zone B, conductive anomalies correspond well to NE-SW trending coincidence raster and NW-SE aspect lineaments (Figure 4.14b). Zone C shows NW-SE alignment along VLF survey anomalies (Figure 4.14c). In Zone H, conductive anomalies are present under N-S and E-W lineament intersections Figure 4.14c. Overall these results show that shallow conductive bodies (such as potential water-bearing fractures or joints) can be identified in VLF-EM surveys. The rest of the VLF-EM Fraser profiles are shown in Appendix C.

Data from VLF surveys generally can be affected by fences, power lines, pipelines, weather, topography and other factors (NGA 2000), which are common in terrains like this area. Some anomalies are present where there is no coincidence or regional aspect trend. This may be due to the conductive bodies being overlain by sand deposits or anthropogenic influences, such as power lines.

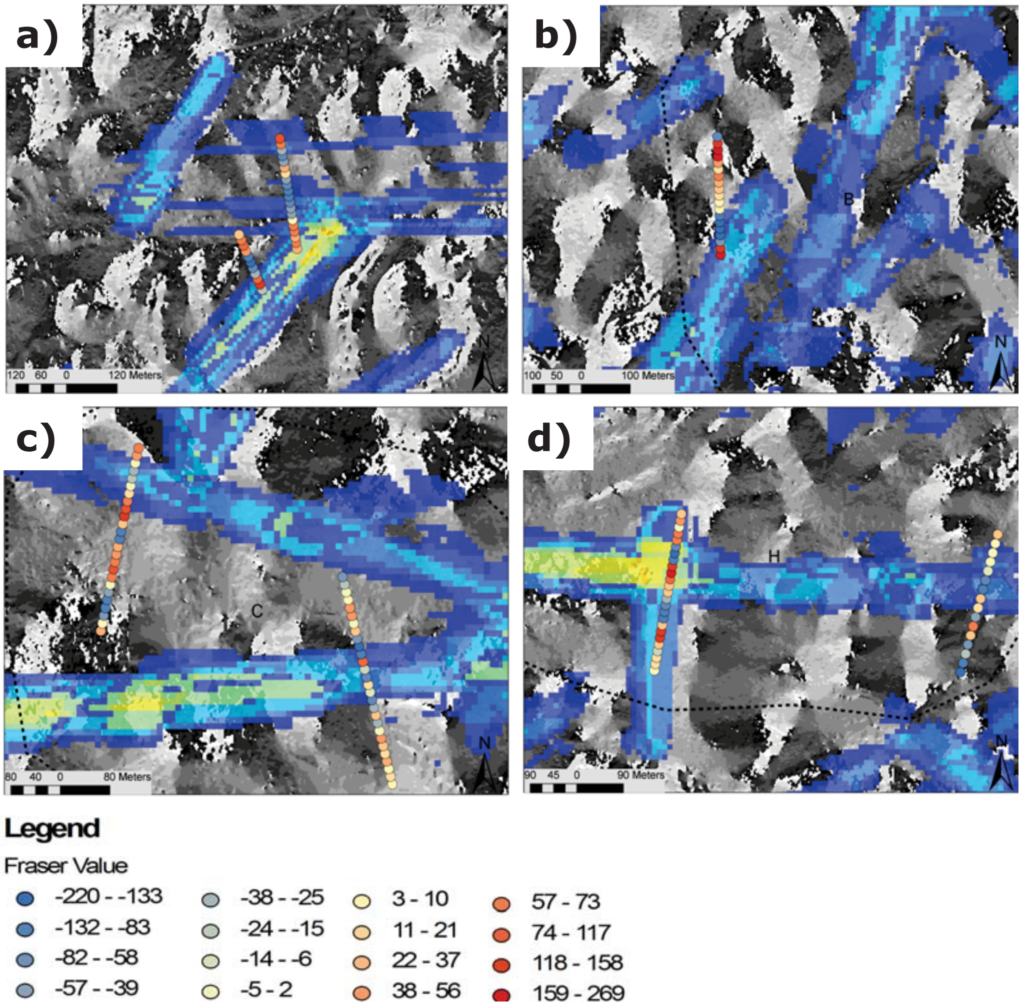

Figure 4.14 Fraser filter values overlaid on aspect map and mapped with Coincidence Raster. a) Zone A. b) Zone B c) Zone C d) from Zone H. Zone locations are shown in Figure 4.12.

4.3.2.Geomorphology and Spring Location

Performing a thorough field campaign on the entire area is challenging due to the rugged terrain and pervasive and dense vegetation. In order to make the most of the field work, the locations visited were based on previously mapped lineaments from the aspect map and from the coincidence raster. For comparison, arbitrary areas that did not lie exactly within the coincidence raster were also visited. However, this area seems to be very influenced by these larger regional features appearing in the RS imagery, so there was some type of geomorphic evidence at most of the places visited. The location and quantity of observed geomorphologic features in the field was influenced by the WADI survey locations, time, and accessibility of the terrain. The field locations for this work are shown in Figure 4.13. Most of the springs and geomorphic features found during the field expedition were along the Eastern river floodplain and correlate well with the lineaments in the coincidence raster (Figure 4.15). Access to these areas was possible via roads available along the river and a more flat topography than the rest of the study area. Therefore, geologic features and springs were visible and readily accessible around the main river.

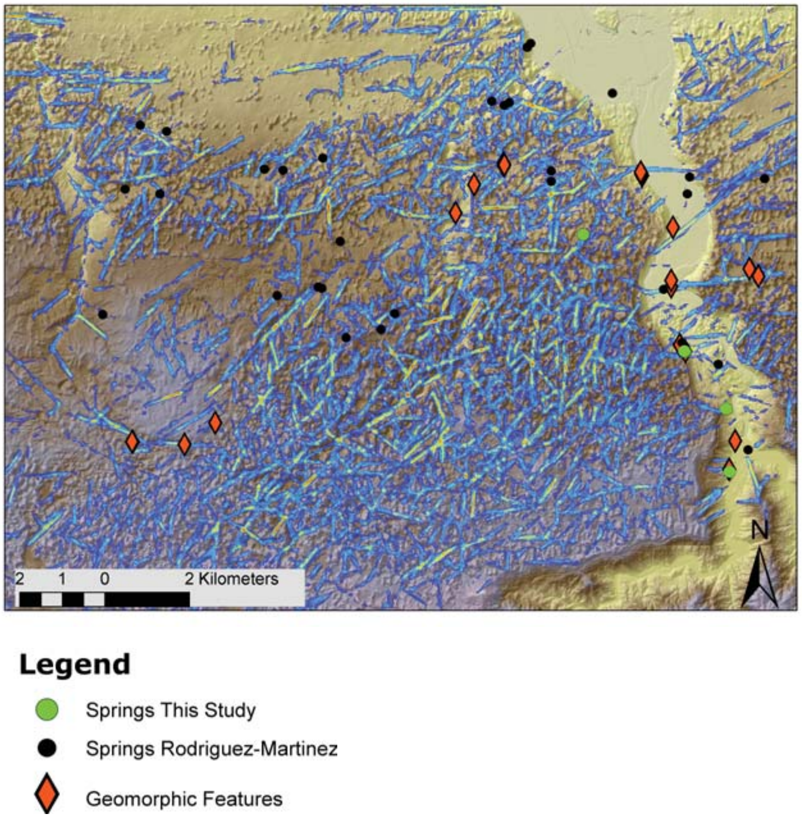

Figure 4.15 Spring location and geomorphic features coupled with the coincidence raster.

Geomorphologic features were analyzed from features found during the field expedition and from the aspect map. The aspect map lets us connect lineaments to see the regional extent of larger lineaments as well as detailed changes in aspect correlated to features of interest. Features found in the field include fractures, discontinuities, caves, saddles, and sinkholes. General strike direction is NE-SW, with others trending W-E and N-S. Those with an azimuth similar to coincident lineaments are shown in Figure 4.16 as red diamonds on the circumference of the Rose diagram. The measured azimuths are plotted to facilitate comparison to the predominant fracture orientations. Example orientations of fractures and discontinuities collected in the field are shown in Figure 4.17.

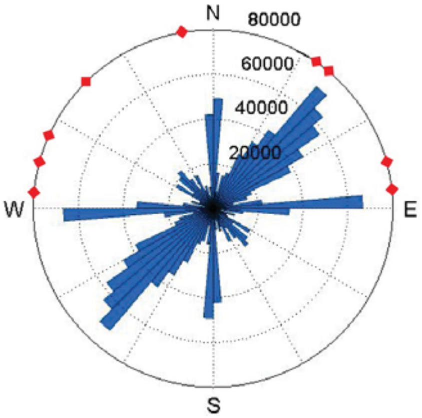

Figure 4.16 Coincidence Analysis lineaments and Field strikes (in red)

Springs found in the field expedition and those from Rodriguez-Martinez (1997) are mapped on the coincidence raster and show correlation to the directional trends (Figure 4.15). This shows that the expression in the surface captured by remote sensing is influencing the hydrology of the area by the presence of springs. Generally, springs show connectivity to lineaments trending NE-SW, NW-SE, and intersections of both, E-W, and minor correlation with NS lineaments.

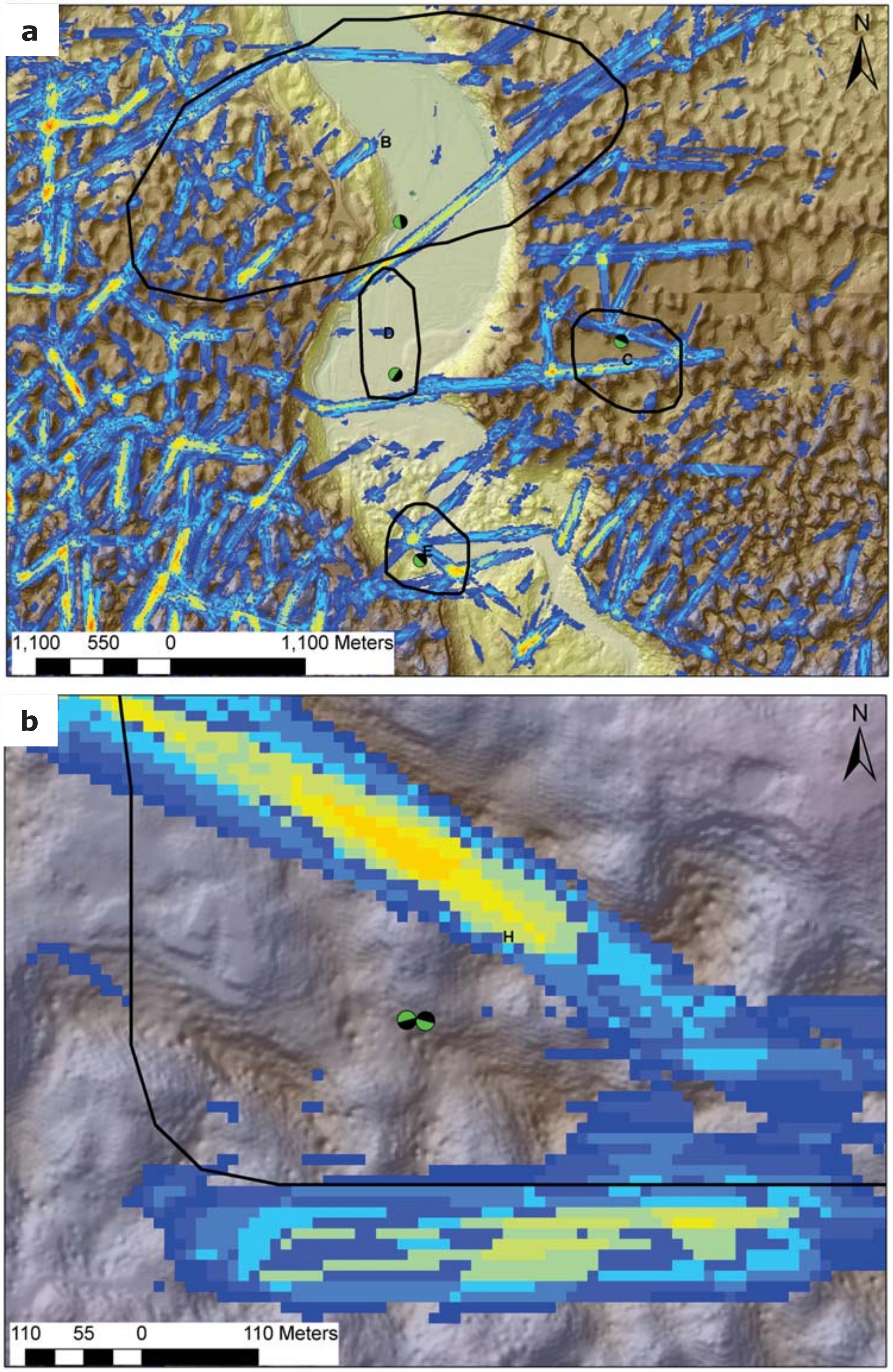

Figure 4.17 Field measured strike (greed and black circles) compared to lineament trends (yellow, green, blue raster). a) includes Zones B, C, D and E. b) includes Zone H

Larger geomorphic features (pictures available in Appendix C), were detected in the remote sensing analysis. Smaller geomorphic features lack sufficient spatial extent to be detectable by remotely sensed imagery.

Other areas that would have been important to conduct field work were too densely vegetated, rugged, and/or developed (i.e., private property). Geomorphic features found during the field campaign represent a small fraction of the total geomorphic features in the area. The discovery of only a few geomorphic features is attributed to their lack of visibility and accessibility.

As shown in Figure 4.15, most springs or geomorphic features can be correlated to areas of dense lineaments, which are highlighted in the coincidence raster. Such geologic evidence in the field shows that the lineaments found using remotely sensed imagery and the aspect map may be affecting topography and hydrology to a significant extent. Electrical conductivity (specific conductance) of water samples were reported by Rodriguez-Martinez (1997). Because, spring electric conductivity (Ec) values (reported in Appendix D) from spring water samples collected during the field campaign do not have a strong correlation to lineaments, such values are not incorporated in to the analyses on this study.

4.3.3.Additional GIS Analysis

To bolster the limited data that could be gained from the field expedition, additional spring locations were obtained from Rodriguez-Martinez (1997) and mapped sinkhole occurrences were taken from Alemán González (2010). These are overlain with lineaments from the Aspect Map. The Aspect Map lineaments were chosen to show how sinkholes are mostly correlated to the NW-SE & NE-SW trending regional geomorphic lineaments. Giusti (1978) found sinkholes aligned in NW- SE direction. A line density map Figure 4.18 (search radius 400 m) shows that sinkhole locations correspond to higher density lineament zones.

4.3.3.1. Lineament Density

A line-density map (Figure 4.18) was prepared in ArcMAP 9.3 to gain a better understanding of the extent of fracturing in the area and its influence on hydrology and geomorphology. The program uses an input search radius (400 m for this case) for each cell and calculates the length (in meters) of lineament segments intersecting that radius and the results are produced in units of m/km^2. A large search radius was chosen in order to produce a smoother generalized raster analysis (Figure 4.18). A high density of interconnected fractures increases secondary porosity and permeability of the rock. A high density of 6 to 9 m/km^2 corresponds well with sinkhole location. Furthermore, this result emphasizes the impact of fracturing is karst topography and hydrology.

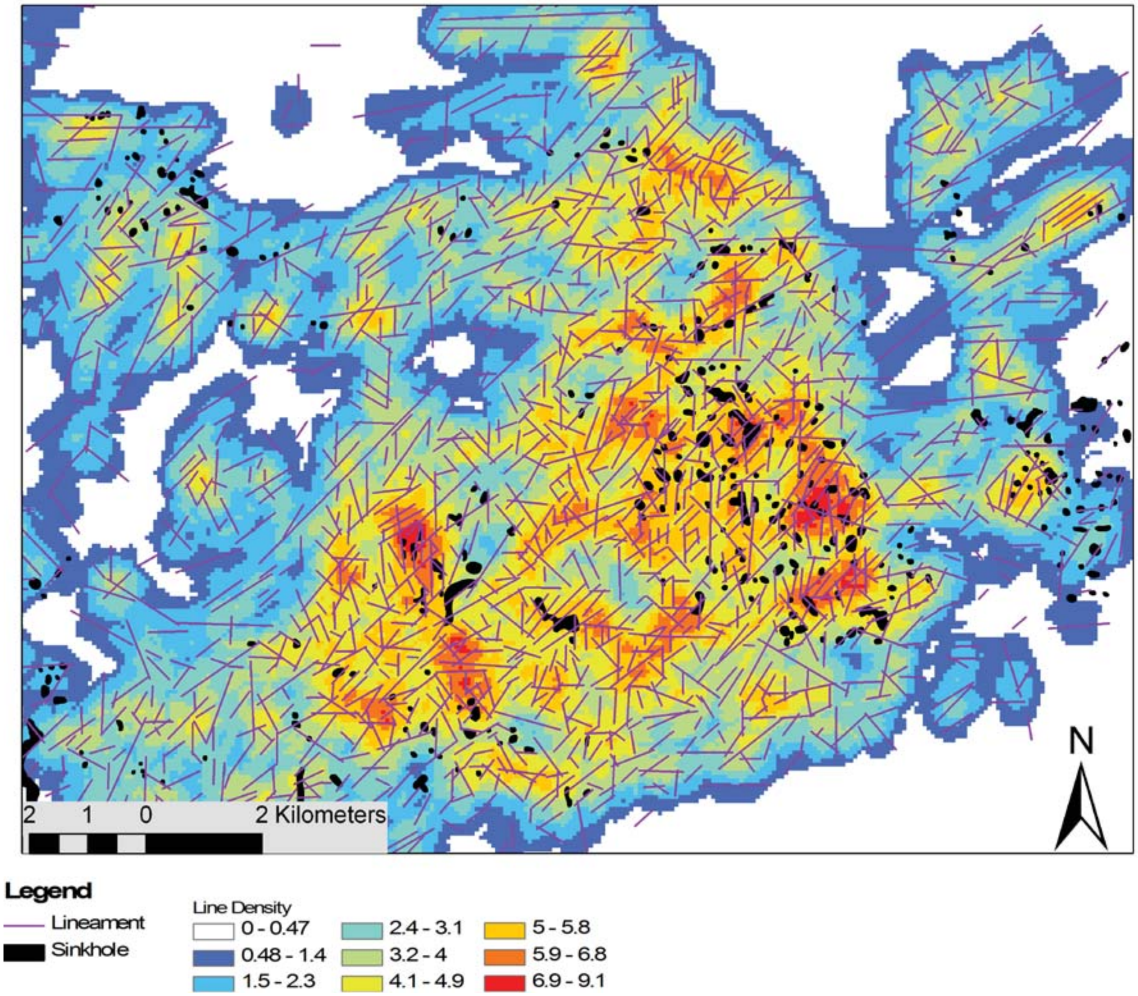

Figure 4.18 Density map and sinkholes polygons from Alemán González (2010)

4.3.3.2. Comparison to NDMI

The NDVI tends to saturate in densely vegetated areas and it is advised to use it to complement the NDMI (Bo-Cai 1996). However, it has been suggested that the NDMI is better related to vegetation water content than the NDVI (Jin and Sader 2005)and is less affected by clouds (Bo-Cai 1996). The NDMI for dry areas, like soils or unhealthy vegetation, should be negative but more positive for healthy vegetation(Bo-Cai 1996). Bo-Cai (1996) found NDMI using MODIS for green vegetation is about 0.064 and -0.056for dry vegetation. In this area, as shown in Figure 4.19, coincident lineaments line up fairly well in zones of higher positive values NDMI (0.2 - 0.6) and high positives in NDVI (0.7). In boundaries of low and high NDMI values, these areas are potential recharge zones for the aquifer system (Figure 4.19). The results of this qualitative assessment show that there is correlation between linear features and denser vegetation locations.

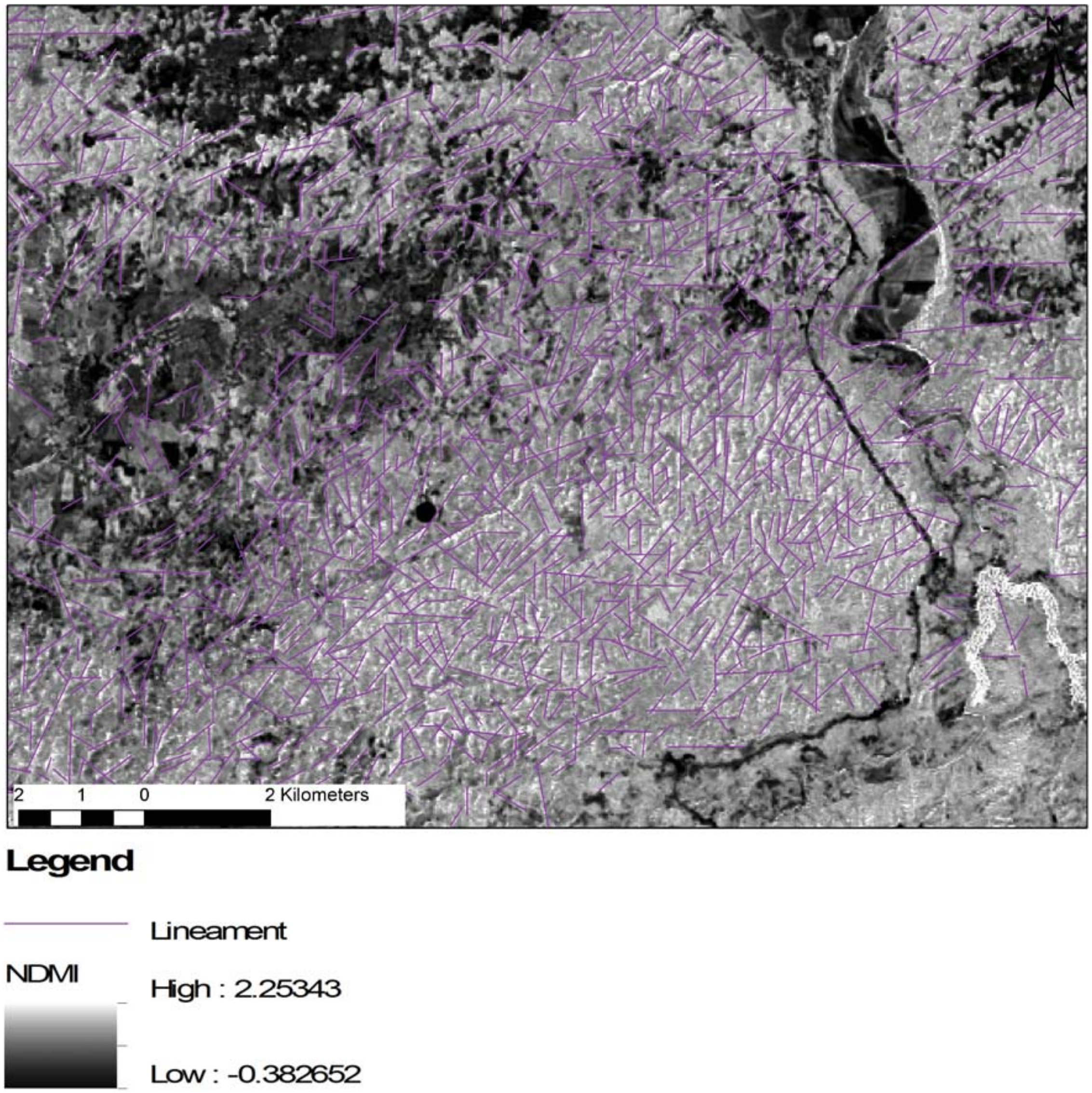

Figure 4.19 NDMI image and coincidence lineaments

5. Conclusions

Groundwater flows in karst systems in complicated networks and it has been shown that it may be possible that regional and local faulting as well as geology and general structure of the area affect its behavior (i.e., flow direction, topography, recharge and discharge, etc.).The Northern Karst Area of Puerto Rico is affected by lineaments, fractures, and faults that may contribute to high vulnerability to transport of contaminants to and within groundwater flows. This is why a better understanding of topographic, hydrological and tectonic connectivity is crucial to address environmental issues. Remote sensing, together with advanced digital image processing and GIS techniques explained herein, is a powerful tool to map lineaments that are controlling the regional karst topography (sinkholes, residual hills) and hydrology (springs, development of groundwater flow conduits).

VLF-EM surveys are a good technique to assess fracturing in karst terrain but should be coupled with others types of geophysical methods, such as airborne techniques, and ground truthing. VLF-EM surveys generally agree with lineament location, possibly signifying fracture control or presence of water flow paths. Field geomorphology data show relation to lineament orientation trends and location. Entire lineament extent cannot be seen in the field, smaller fracture and joint sets found on the field can be related to larger coincident lineaments that extend in the area. The fact that the presence of lineaments, faults and fractures, show a very possible influence on the occurrence of springs and sharp river-course changes, may indicate that tectonics may be strongly controlling the hydrology of the karst system.

ASTER VNIR bands, Landsat ETM+ & TM PCA and high-resolution LiDAR DEM are shown to be proficient in enhancing lineaments for this type of terrain, as shown in the % Coincidence and False Identification % values. Even though Landsat ETM+ & TM Thermal and RADARSAT-1 imagery did not have such good ranking in the image assessment, they were valuable for detecting regional features important for this type of terrain.

Remote sensing and GIS techniques used in volcanic terrains can be adjusted in small ways so that they can be applied to karst terrains. Similar to hard-rock terrains, several types of images are necessary to make a more accurate lineament map. There are features that appear in one type of image and that would not appear in another type. The spatial, spectral and temporal resolution of the image influences the ability to identify lineaments, especially in karst terrains. A high spatial-resolution LiDAR DEM is favorable in densely vegetated conditions as well as using various optical sensors with similar spectral resolution at different seasons.

Landsat ETM + and LiDAR products (NDMI & Aspect, respectively) are important assets when interpreting lineaments. Coupled with coincidence analysis using different sensor types and their products help establish the connectivity of vegetation, topography, hydrology and interpreted lineaments. ASTER VNIR bands, Landsat ETM+ & TM PCA and High resolution LiDAR DEM are shown to be valuable tools in enhancing lineaments for this type of terrain. Even though Landsat ETM+ & TM Thermal and RADARSAT-1 imagery were not ranked as highly, they were valuable for detecting regional features important for this type of terrain.

Lineaments interpreted from topographic features (ridgelines, slope breaks, etc.), should not be solely attributed to faulting/fracturing. These may in some instances may also be caused by wind erosion, bedding planes or other geologic phenomena (Jordan et al. 2005).

Lineaments found in this study area are affecting not only topography but also hydrology. This influence on the hydrology was observed in the following factor’s correlation to lineament location and extent: NDMI high moisture areas, the occurrence of springs, and the pattern of sharp river channel turns.

In addition, digital terrain analysis and field data; help us corroborate the importance of performing a coincidence analysis in order to determine if and how lineaments detected by RS in various parts of the EM spectrum are affecting the geomorphotechtonics and hydrology of an area.

6. Future Work

The methodology used here is only a start for the countless possible remote sensing from groundwater applications in tropical karst systems. To further quantify the degree of fracturing and its influence in groundwater flow velocity and direction, some possible future studies are suggested below:

-Apply a change detection tool with two overlapping scenes. This would involve two scenes available of a given sensor, one from the dry season and another from wet season. Change detection can enhance changes in vegetation trends, which can be associated to lineaments due to changes in water availability, making lineament interpretation feasible. Moreover, edge enhancement filters could be applied. Bruning et al. (2011) applied this technique using RADARSAT-1 scenes from different seasons. Incorporating scenes from different sensors and making side-to-side comparisons of the change detection products of each sensor can help us determine which sensor would be the practical choice for this type of analysis.

-Use of Multidirectional Oblique Weighting (MDOW), an ArcGIS tool, used to integrate various hill shades of different sun illumination angles. In this manner, relief information from a number of hillshades can be incorporate into a single hillshade from which lineaments can be interpreted. This method helps minimize the number of elevation-derived products (hillshades) for manual lineament digitizing.

- Perform flow measurements on springs and/or pumping tests in available wells (if any), in order to assess the connectivity of fractures and the influence on the productivity of the aquifer. Both of these approaches may be labor intensive in this type of terrain but highly necessary to quantitatively characterize its hydrology.

- Tracer studies (e.g., stable isotopes) might help us have a better understanding of the connectivity of flow direction and velocity in the flow network.

- Expand the study area to the entire Northern Karst system in order to map regional lineaments and fracture characterization. This will help determine that if geological and tectonic conditions are similar across the entire karst region, then fracturing and faulting are most likely controlling (to an extent) the hydrology of the karst groundwater system. Acquiring a high resolution LiDAR DEM for the entire area can be used to carry out quantitative analyses as sinkhole location and depth, supplementing the study of suffusion and other karst related hazards.

-Execute surface geophysics surveys, by coupling VLF-EM and 2D geoelectrical surveys results, to make more quantitative analysis of the fracturing (depth, extent).2 D geoelectrical surveys will also help determine resistivity changes along geologic layers. Airborne gravity surveys, as suggested by Bruning (2008), may also be used in addition to or instead of ground based surveys.

-The use of two or more lineament interpreters for all remote sensing images may reduce the subjectivity of final lineament map.

7. Reference List

ABEM. 1989. WADI VLF Instrument. Interpretation Guide. Instruction manual provided with the ABEM AB. Bromma, Sweden.

Al-Tarazi E, Abu Rajab J, Al-Naqa A, El-Waheidi M. 2008. Detecting leachate plumes and groundwater pollution at Ruseifa municipal landfill utilizing VLF-EM method. Journal of Applied Geophysics 65:121–131.

Alemán González W. 2010. Karst map of Puerto Rico: U.S. Geological Survey Open-File Report 2010–1104, 1 map sheet, scale 1:140,000, available online at http://pubs.usgs.gov/of/2010/1104. In: USGS, editor.

Bawiec W. 1998. Geology, geochemistry, geophysics, mineral occurrences, and mineral resource assessment for the commonwealth of Puerto Rico. In: (U.S.) GS, editor.

Begg J, Mouslopoulou V. 2010. Analysis of late Holocene faulting within an active rift using lidar, Taupo Rift, New Zealand. Journal of Volcanology and Geothermal Research 190 152-167.

Benson R, Yuhr L. 1993. Spatial sampling considerations and their applications to characterizing fractured rock and karst systems Environmental Geology 22:296-307.

Bo-Cai G. 1996. NDWI A Normalized Difference Water Index for Remote Sensing of Vegetation Liquid Water From Space. Remote Sensing of Environment 58:257-266.

Bruning J. 2008. A digital processing data compilation approach for using remotely sensed imagery to identify geological lineaments in hard-rock terrains: an application for groundwater exploration in Nicaragua. [Houghton]: Michigan Technological University.

Bruning J, Gierke J, Maclean A. 2011. An Approach to Lineament Analysis for Groundwater Exploration in Nicaragua. Photogrammetric Engineering & Remote Sensing 77(5):1-11.

Carter W, Shrestha R, Tuell G, Bloomquist D, Sartori M. 2001. Airborne Laser Swath Mapping Shines New Light on Earth’s Topography Eos, Transactions, American Geophysical Union 82(46): 549, 550, 555.

Landsat Vegetation Indices [Internet]. 2004. Tucson, AZ: University of Arizona. [updated 16/Mar/2004, cited 21/Dec/2011]. Available from:

http://arsc.arid.arizona.edu/resources/image_processing/vegetation/index.html

Chavez P. 1996. Image-based atmospheric corrections - Revisited and Improved. . Photogrammetric Engineering and Remote Sensing 62(9):1025-1036.

Della Seta M, Del Monte M, Fredi P, Palmieri A. 2004. Quantitative morphotechtonic analysis as a tool for detecting deformation patterns in soft-rock terrains: a case study from the southern Marches, Italy Géomorphologie : relief, processus, environnement 10(4):267-284.

Dixon CR. 2004. LiDAR system calibration FOR: SE Peñuelas and SW Poncé Quads Contract No. DACW43-03-D-0504. St. Louis CORPS of Engineers and the 3001 Spatial Data Company. p. 33.

Djeddi M, Baker H, Tabbagh A. 1998. Interpretation of VLF-EM anomalies of 3D structures by using linear filtering techniques. Annali di Geofisica 41(2):151-163.

Easterbrook D. 1999. Surface Processes and landforms. Upper Saddle River, NJ: Prentice-Hall, Inc.

Edet A, Okereke C, Teme S, Esu E. 1998. Application of remote-sensing data to groundwater exploration: A case study of the Cross River State, southeastern Nigeria. Hydrogeology Journal 6:394-404.

Escobar-Wolf R. 2011. Rose diagram Matlab Script. In: diagram Pwr, editor. MATLAB. Houghton.

Evans J, Hudak A. 2007. A multiscale curvature algorithm for classifying discrete return LiDAR in forested environments. . Geoscience and Remote Sensing 45(4):1029-1038.

Gao B-C. 1996. NDWI A Normalized Difference Water Index for Remote Sensing of Vegetation Liquid Water From Space. Remote Sensing of Environment 58:257-266.

Giusti E. 1978. Hydrogeology of the Karst of Puerto Rico. In: INTERIORCECIL USDOT, editor. GEOLOGICAL SURVEY PROFESSIONAL PAPER WASHINGTON UNITED STATES GOVERNMENT PRINTING OFFICE. p. 1-65.

Guérin R. 2005. Borehole and surface-based hydrogeophysics. Hydrogeology Journal 13:251-254.

Harding DJ, Berghoff GS. Fault scarp detection beneath dense vegetation cover: Airborne lidar mapping of the Seattle fault zone, Bainbridge Island, Washington State. American Society of Photogrammetry and Remote Sensing Annual Conference; 2000; Washington, D.C. p. 9.

Haugerud R, Harding D, Johnson S, Harless J, Weaver C, Sherrod BL. 2003. High-Resolution Lidar Topography of the Puget Lowland, Washington-A Bonanza for Earth Science. GSA TODAY 4-10.

Hawbaker T, Keuler N, Lesak A, Gobakken T, Contrucci K, Radeloff V. 2009. Improved estimates of forest vegetation structure and biomass with a LiDAR-optimized sampling design. Journal of Geophysical Research 114(G00E04):1-11.

Hung L, Dinh N, Batelaan O, Tam V, D. L. 2002. REMOTE SENSING AND GIS-BASED ANALYSIS OF CAVE DEVELOPMENT IN THE SUOIMUOI CATCHMENT. Journal of Cave and Karst Studies 64(1):23-33.

Hung L, Batelaan O. 2003. Environmental Geological Remote Sensing and GIS Analysis of Tropical Karst Areas in Vietnam. IEEE:2964-2966.

Hung L, Batelaan O, De Smedt F. 2005. Lineament extraction and analysis, comparison of LANDSAT ETM and ASTER imagery. Case study: Suoimuoi tropical karst catchment, Vietnam. Remote Sensing for Environmental Monitoring, GIS Applications, and Geology: Proc. of SPIE 5983:12.

Hunter J, Arbona S. 1995. Paradise lost: An introduction to the geography of water pollution in Puerto Rico. Soc. Sci. Med. 40(10):1331-1355.

Interpex. 2010. IXVLF VLF Data Presentation and Processing Package Golden, Colorado.

Jensen J. 2007. Remote Sensing of the environment; An earth resource perspective. Upper Saddle River, NJ: Pearson Prentice Hall.

Jin S, Sader S. 2005. Comparison of time series tasseled cap wetness and the normalized difference moisture index in detecting forest disturbances. Remote Sensing of the Environment 94:364-372.

Jones IC, Banner JL, Humphrey JD. 2000. Estimating recharge in a tropical karst aquifer. Water Resources Research 36(5):1289-1299.

Jordan G, Meijninger BML, van Hinsbergen DJJ, Meulenkamp JE, van Dijk PM. 2005. Extraction of morphotectonic features from DEMs: Development and applications for study areas in Hungary and NW Greece. International Journal of Applied Earth Observation and Geoinformation 7:163–182.

Karnieli A, Meisels A, Fisher L, Arkin Y. 1996. Automatic Extraction and Evaluation of Geological Linear Features from Digital Remote Sensing Data Using a Hough Transform Photogrammetric Engineering & Remote Sensing 62(5):525-531.

Kazemi R, Porhemmat J, M. K. 2009. Investigations of Lineamnets Related to ground Water Occurrence in a Karstic Area: A Case Study in Lar Catchment, Iran. Rsearch Journal of environmental Sciences 3(3):367-375.

Kocal A, Duzgunb HS, Karpuza C. DISCONTINUITY MAPPING WITH AUTOMATIC LINEAMENT EXTRACTION FROM HIGH RESOLUTION SATELLITE IMAGERY. Geo-Imagery Bridging Continents XXth ISPRS Congress; 2004; Istanbul, Turkey.

Koike K, Shuishi N, Michito O. 1995. LINEAMENT ANALYSIS OF SATELLITE IMAGES USING A SEGMENT TRACING ALGORITHM (STA). Computers & Geosciences 21(9):1091-I 104

Korpela IS. 2008. Mapping of understory lichens with airborne discrete-return LiDAR data. Remote Sensing of Environment 112:3891-3897.

Koutepov V, Mironov O, VV. T. 2008. Assessment of suffosion-related hazards in karst areas using GIS technology. Environ Geol 54:957-962.

Kresic N. 1995. Remote Sensing of Tectonic Fabric Controlling Groundwater Flow in Dinaric Karst. Remote Sensing of the Environment Volume 53:85-90.

Lee TH, Moon WM. 2002. Lineament Extraction from Landsat TM, JERS-1 SAR, and DEM for Geological Applications. IEEE 6:3276-3278.

Leica-Geosystems. ALS50 Airborne Laser Scanner [Internet]. Atlanta, Georgia 30329, USA2004. Available from: http://www.geos.unicaen.fr/projets/clarec/documents/ALS50_brochure.pdf

Leica Geosystems Geospatial Imaging L. 2006. ERDAS IMAGINE. 9.1. ed.

Lugo A, Miranda Castro L, Vale A, del Mar López T, Hernández Prieto E, García Martinó A, Puente Rolón AR, Tossas AG, McFarlane DA, Miller T et al. . 2001. Puerto Rican Karst, A Vital Resource: General Technical Report WO-65. In: Tech. USDoAFSG, editor.

Meijerink A, Bannert D, Batelaan O, Lubczynski M, Pointet T. 2007. Remote Sensing Applications to Groundwater. Paris, France: IHP-VI. p. 304.

Monroe W. 1966. Formation of Tropical Karst topography by Limestone solution and reprecipitation. Carib. 1. Sci. 6(1-2):1-7.

Monroe W. 1980. Geology of the middle tertiary formations of Puerto Rico. In: U.S.Geological-Survey, editor. p. 93.

Monteiro-Santos FA, Mateus A, Figueiras J, Gonçalves MA. 2006. Mapping groundwater contamination around a landfill facility using the VLF-EM method — A case study. Journal of Applied Geophysics 60:115–125.

NGA. 2000. VLF Method. In: Northwest Geophysical Associates I, editor. Geophysical Services: Environmental, Groundwater, Geotechnical. p. 2.

Offield T. 1975. Thermal-Infrared Images as a Basis for Structure Mapping, Front Range and Adjacent Plains in Colorado. Geological Society of America Bulletin 86:495-502.

Ramli MF, Tripathi NK, Yusof N, Shafri HZM, Ali Rahman z. 2009. Lineamnent mapping in a tropical environment usinf Landsat imagery. International journal of Remote Sensing 30(23-24):6277-6300.

Remmel T, Todd K, J. B. 2008. A comparison of existing surficial hydrological layers in a low-relief forested Ontario landscape with those derived from a LiDAR DEM. The forestry chronicle 84(6):850-865.

Renken R, Ward W, Gill I, Gómez-Gómez F. 2002. Geology and Hydrogeology of the Caribbean Islands Aquifer System of the Commonwealth of Puerto Rico and the U.S. Virgin Islands. In: SURVEY USG, editor. Reston, Virginia: Library of Congress Cataloging-in-Publication Data. p. 139.

Rinker J. An Aplication of air photo analysis to cave location study. 40th Annual meeting American Society of Photogametry; 1974; St louis, mo p. 281-289.

Rios-Sanchez M, Gierke JS, McLean A, Muñoz-Martínez T. Identification and characterization of fracturing patterns and their influence on the hydrology of the plateaus region of the Quito aquifer system, based on remote sensing, digital morphological analysis and geophysics. 2012 World Environmental & Water Resources Congress, American Society of Civil Engineers; in Preparation; Albuquerque, NM.

Rodriguez-Martinez J. 1997. Characterization of Springflow in the North Coast Limestone of Puerto Rico using physical, chemical and stable isotopic methods. In: Interior USDo, editor. San Juan, PR.

Salvati R, Sasowsky I. 2002. Development of collapse sinkholes in areas of groundwater discharge. Journal of Hydrology 264:1-11.

Sander P, Minor T, Chesley M. 1997. Ground-Water Exploration Based on Lineament Analysis and Reproducibility Tests. Ground Water 35(5):888-894.

Sankar K. 2002. Evaluation of Groundwater Potential Zones Using Remote Sensing Data In Upper Vaigai River Basin, Tamil Nadu, India. Journal of the Indian Society of Remote Sensing 30(3):119 -129.

Sesôren A. POTENTIAL OF REMOTE SENSING USE IN A KARSTIC AREA, ANTALYA REGION IN THE SOUTH OF TURKEY. Karst Water Resources: Proceedings of the Ankara - Antalya Symposium [Internet].161:271-357.

Shaban A, Khawlie M, Abdallah C. 2006. Use of remote sensing and GIS to determine recharge potential zones: the case of Occidental Lebanon. Hydrogeology Journal 14:433-443.

Sherrod B, Brocher T, Weaver C, Bucknam R, Blakely R, Kelsey H, Nelson A, Haugerud R. 2004. Holocene fault scarps near Tacoma, Washington, USA. Geology 32:9-12.

Warehouse Inventory Search Tool (WIST) [Internet]. 2009. Sioux Falls, SD: USGS. [updated 06/Oct/2009, cited 21/Dec/2011]. Available from: https://lpdaac.usgs.gov/lpdaac/get_data/wist

Tam V, De Smedt F, Batelaan O, Dassargues A. 2004. Study on the relationship between lineaments and borehole specific capacity in a fractured and karstified limestone area in Vietnam. Hydrogeology Journal 12:662-673.

Seamless Data Warehouse [Internet]. 2010 USGS. [updated 28/Dec/2010 cited 21/Dec/2011]. Available from: http://seamless.usgs.gov/

EarthExplorer [Internet]. 2011a. USGS. [updated 09/20/2011 cited 21/Dec/2011]. Available from: http://edcsns17.cr.usgs.gov/NewEarthExplorer/

National Hydrography Dataset [Internet]. 2011b. USGS. [updated 01/Sep/2011, cited 21/Dec/2011]. Available from: http://nhd.usgs.gov/wbd.html

Vassilas N, Perantonis S, Charou E, Tsenoglou T, Stefouli M, Varoufakis S. Delineation of Lineaments from Satellite Data Based on Efficient Neural Network and Pattern Recognition Techniques. 2nd Hellenic Conf. on AI; 2002; Thessaloniki, Greec. p. 355-366.

Ward W, Scharlach R, Hartley J. 1991. Controls on porosity and permeability in subsurface Tertiary carbonate rocks of northern Puerto Rico in Gómez-Gómez, Fernando, Quiñones-Aponte, Vicente, and Johnson, A.I. eds., Regional aquifer systems of the United States: Aquifers of the Caribbean Islands. American Water-Resources Association 15:17-23.

Wladis D. 1999. Automatic Lineament Detection Using Digital Elevation Models with Second Derivative Filters. Photogrammetric Engineering & Remote Sensing 65(4):453-458.

Yilmaz I. 2007. GIS based susceptibility mapping of karst depression in gypsum: A case study from Sivas basin (Turkey). Engineering Geology 90:89-103.

Appendix A.

Table A.1
Statistics for ASTER image VNIR bands.

1. EIGENVECTORS			
	PC1	PC2	PC3
B1	0.4726	0.5464	-0.6914
B2	0.3905	0.5735	0.7201
B3	0.7901	-0.6103	0.0577
2. EIGEN VALUES			
	212.755924	114.625818	1.331527
Difference	98.1301	113.2943	1.3315
Total Variance	328.7133		
% Variation	**64.7239**	**34.8711**	**0.4051**
3. COVARIANCE MATRIX			
	B1	**B2**	**B3**
B1	82.3784	74.5207	41.1555
B2		70.8342	25.5690
B3			175.5007
4. FACTOR LOADINGS			
	PC1	**PC2**	**PC3**
B1	0.759	0.645	-0.088
B2	0.677	0.730	0.099
B3	0.870	-0.493	0.005

Table A.2
Eigen vectors for Landsat ETM + image

	PC1	PC2	PC3	PC4	PC5	PC6	Pc7
B1	0.43828872	-0.017572	0.539094	-0.265001	-0.627989	0.023252	-0.22767
B2	0.36135567	0.178653	0.31905	-0.088551	0.270477	-0.253401	0.768441
B3	0.35270691	0.273898	0.306393	0.163696	0.62699	0.096452	-0.52677
B4	0.37477977	0.33746	-0.579142	-0.606964	0.028726	0.200583	-0.02815
B5	0.31529856	0.299799	-0.34892	0.488056	-0.272864	-0.601739	-0.11924
B6	0.51499241	-0.807944	-0.226067	0.093849	0.148475	0.007103	0.000421
B7	0.21870683	0.19032	-0.073837	0.528891	-0.205012	0.723582	0.255279

Table A.3
Eigen values Statistics for Landsat ETM + image

	8156.55553	2348.165	688.5343	130.2485	39.83406	11.95015	7.88844
Difference	5808.3902	1659.6311	558.2857	90.4145	27.8839	4.0617	7.8884
Total Variance	11383.1764						
% Variation	**71.6545**	**20.6284**	**6.0487**	**1.1442**	**0.3499**	**0.1050**	**0.0693**

Table A.4
Cobariance matrix for Landsat ETM + image

	B1	**B2**	**B3**	**B4**	**B5**	**B6**	**b7**
B1	1792.94959	1397.715	1342.966	1131.255	975.3119	1783.533	733.2163
B2	1397.71452	1219.461	1223.166	1125.507	970.9647	1129.797	699.2879
B3	1342.96602	1223.166	1276.94	1161.182	1029.676	919.9563	741.9507
B4	1131.25506	1125.507	1161.182	1692.518	1300.228	1016.976	808.4539
B5	975.311851	970.9647	1029.676	1300.228	1144.177	814.2682	744.5855
B6	1783.53287	1129.797	919.9563	1016.976	814.2682	3733.293	574.4268
b7	733.216341	699.2879	741.9507	808.4539	744.5855	574.4268	523.8375

Table A.5

factor loadings for Landsat ETM + image

	PC1	**PC2**	**PC3**	**PC4**	**PC5**	**PC6**	**Pc7**
B1	0.935	-0.02	0.334	-0.071	-0.094	0.002	-0.015
B2	0.935	0.248	0.24	-0.029	0.049	-0.025	0.062
B3	0.891	0.371	0.225	0.052	0.111	0.009	-0.041
B4	0.823	0.397	-0.369	-0.168	0.018	0.017	-0.002
B5	0.842	0.429	-0.271	0.165	-0.051	-0.061	-0.01
B6	0.761	-0.641	-0.097	0.018	0.015	0	0
b7	0.863	0.403	-0.085	0.264	-0.057	0.109	0.031

Table A.6

Eigen vectors for Landsat TM image

	PC1	PC2	PC3	PC4	PC5	PC6	**thermal**
B1	0.36098156	-0.328737564	-0.545957	0.640276	0.03178	0.133129	0.1867304
B2	0.24686182	-0.163430474	-0.288057	-0.25275	0.055629	0.15366	-0.8595255
B3	0.30782543	-0.299450954	-0.301763	-0.71758	0.016521	-0.006079	0.4574717
B4	0.34496572	0.859285697	-0.349139	-0.038824	-0.092892	-0.094294	0.0412476
B5	0.6884049	0.030459819	0.606767	0.057209	0.242902	0.304907	0.0419812
B7	0.34458967	-0.187314541	0.172592	0.07842	-0.354127	-0.819412	-0.1157248
th	0.04848064	-0.034128763	0.089675	-0.017676	-0.895872	0.430503	0.0145388

Table A.7

Eigen Values for Landsat TM image

	738.234325	270.8208267	70.58452	7.539592	5.546268	4.05718	1.0519819
Difference	467.4135	200.2363	63.0449	1.9933	1.4891		
Total Variance	1096.7827						
% Variation	**67.3091**	**24.6923**	**6.4356**	**0.6874**	**0.5057**	**0.3699**	

Table A.8

Covariance matrix for Landsat TM image

	B1	**B2**	**B3**	**B4**	**B5**	**B7**	**thermal**
B1	149.7089	90.1404	116.9461	28.6360	157.8500	101.7056	12.4944
B2		59.4507	76.4432	31.8830	111.8891	66.9152	8.5350
B3			104.7689	16.3669	140.7693	89.3294	11.8847
B4				296.5186	167.1916	40.3793	2.4969
B5					376.8192	179.5065	27.5158
B7						102.7444	15.4728
th							7.8240

Table A.9

Factor loadings for Landsat TM image

	PC1	**PC2**	**PC3**	**PC4**	**PC5**	**PC6**	**thermal**
B1	0.802	-0.442	-0.375	0.144	0.006	0.022	0.0156529
B2	0.870	-0.349	-0.314	-0.090	0.017	0.040	-0.1143363
B3	0.817	-0.481	-0.248	-0.192	0.004	-0.001	0.0458408
B4	0.544	0.821	-0.170	-0.006	-0.013	-0.011	-0.0056165
B5	0.964	0.026	0.263	0.008	0.029	0.032	0.0022182
B7	0.924	-0.304	0.143	0.021	-0.082	-0.163	-0.0117099
therm	0.470922	-0.2007917	0.269345	-0.017352	-0.754276	0.310008	0.0053311

Appendix B.

Table B.1
LMAX and LMIn values for Landsat ETM+ image used in DN convertion to At-sensor reflectance

Band #	LMAX	LMIN
1	191.600	-6.200
2	196.500	-6.400
3	152.900	-5.000
4	157.400	-5.100
5	31.060	-1.000
7	10.800	-0.350

Appendix C.

CD ROM including products used for delineating lineaments, photographs of geomorphic features and VLF Surveys

Table C.1

CD ROM Products used for delineating lineaments

Sensor	Processing Level	File Name (.jpg)
RADARSAT-1	Despeckle - 3rd	radardesp3
ASTER	Combination of Bands 1,2 &3	Asteroriginal321
	Combination of VNIR PCA	AsterPCA
Landsat ETM+	Reflectance Combination of Bands 1-5 and 7	landsatetmoriginal473
	Thermal Band	thermaletm
	Panchromatic band	landsatpan
	NDWI	landsatndmi
	NDVI	landsatndvi
	PCA Visible + Thermal band Combination	landsatetmpca
Landsat TM	Reflectance Combination of Bands 1-5 and 7	lsattm743
	PCA Visible + Thermal band Combination	lsattmpca
Lidar DEM	Mosaic	lidardem
	HS 275 Azimuth	LidarHS275
NED DEM	HS 315 Azimuth	LidarHS315
	Aspect Map	asplidar
	Mosaic	neddem
	HS 275 Azimuth	nedhs275
	HS 315 Azimuth	nedhs315

Table C.2

CD-ROM pictures and XY coordinates of geomorphic locations located in geomorphology photos by zone. Figures showing feature strike and CR are located within geomorphology photos folder.

Waypoint	POINT_X	POINT_Y	Type	Strike
034	746293.623388	2028859.592130	Sadle vocanic	
041	746842.434683	2032748.127980	Fracture	
050	745124.046605	2030968.945840	hills aligned	
053	744990.266902	2031125.873550	bedding plane	315
075	744086.793796	2035171.423100	joints	
078	744107.144587	2035120.679410	fracture	
079	744086.797773	2035138.724240	fracture	
080	744072.651626	2035206.134450	fracture	
081	744828.912631	2033899.664530	hills alignment	
082	744787.459740	2032499.512470	fracture cave	
089	739712.157496	2034243.055210	joint	
094	740841.888005	2035408.684590	fracture	84
095	740847.926269	2035363.062680	fracture	75
096	740857.782861	2035378.688540	fracture	40
101	740145.704091	2034912.414940	fracture	
105	744789.187150	2032646.807200	fracture	35
109	733326.915130	2028777.215090	cave small	
111	734050.501471	2029283.816050	karst topography	
115	732108.717578	2028836.119850	fracture	285
122	739939.437024	2040630.593120	CAVE	
132	746633.000000	2032921.000000	fracture	294
137	746151.000000	2028184.000000	hills alignment	275
116	732092.033503	2028836.881840	fracture	75

Table C.3

VLF-EM surveys start and end points Fraser values for these transects made are available in the folder named VLF in the excel spreadsheet. In addition figures of Fraser anomalies for each transect are located under the its respective zone folder

Wadi #	Easting	Northing	
200	746864.2248	2032560.672	start
200	746783.6933	2032895.236	end
202	747066.8765	2036710.772	start
202	747074.0813	2036980.755	end
203	746672	2036770	start
203	746664	2036921	end
204	746302	2036404	start
204	746240.1937	2036747.645	end
206	736951.4773	2038871.62	start
206	736896.6403	2039001.089	end
207	737034.2611	2038968.07	start
207	736993.635	2039226.644	end
208	738795.1087	2039028.884	start
208	738745.2019	2039234.823	end
209	746154.4375	2034748.038	start
209	746180.0975	2034958.659	end
210	746879	2033984	start
210	746934.2276	2034116.102	end
211	746392	2032809	start
211	746453.076	2033103.763	end
212	746306.4303	2034790.495	start
212	746299.4159	2034892.146	end
213	744151.6443	2035102.001	start
213	744083.5016	2035176.763	end
214	744222.674	2034959.963	start
214	744072.4449	2035205.407	end
215	744785.1729	2032492.297	start
215	744743.3642	2033015.933	end
216	744725.0383	2032520.243	start
216	744702.5083	2032963.158	end
219	739723.2216	2034081.808	start
219	739699.7094	2034284.954	end
220	739641.4767	2034202.465	start
220	739695.8873	2034378.482	end
222	742715.267	2033717.002	start
222	742708.6264	2033955.309	end

Table C.3 Continued

224	733287.1081	2028592.036	start
224	733339.8076	2028893.796	end
226	733879.8561	2028588.647	start
226	733951.6164	2028854.347	end
227	732583.1342	2029377.302	start
227	732532.089	2029638.443	end
230	739874.9464	2040467.6	start
230	739936.992	2040682.262	end
231	738802.7539	2039874.363	start
231	738798.7722	2040011.273	end
232	736536.1701	2037817.243	start
232	736511.0793	2037994.316	end
233	736575.3944	2037813.664	start
233	736535.8629	2037990.115	end

Appendix D.

Electric conductivity field values were taken from (Rodriguez-Martinez 1997) Spring Electric conductivity (Ec) and from spring water samples of the field campaign. When mapped in ArcGIS there is a slight possible NE trend of increasing Ec. There is also a lower Ec trend within the springs along the Rio Grande de Arecibo. Temperature values show no trend. There is also a slight proportionally direct trend shown in Figure D.1

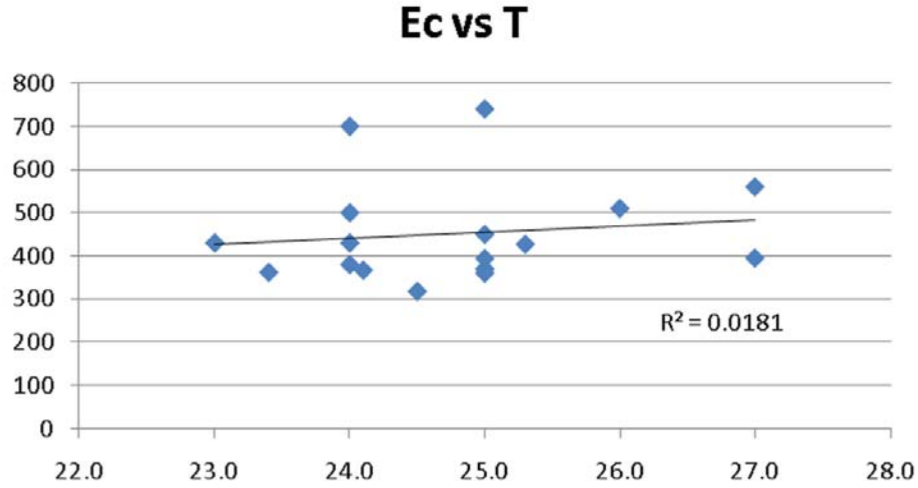

Figure D.1 Ec µS/m and Temperature (˚C) values taken from springs from (Rodriguez-Martinez 1997) and from field expedition

Table D.1
Ph, Electric Conductivity (Ec) in µS/m, temperature (˚C) and location of field collected springs

waypoint	POINT X	POINT Y	pH	Ec (µS/m)	Temp ˚C
035	745126.262888	2030957.668430			
048	746166.304921	2028132.779220	8.4	427.0	25.3
049	746085.678592	2029617.570940	9.3	210.0	28.3
051	745096.940276	2030967.769610	8.3	367.0	24.1
052	745093.019253	2030979.235670	8.2	362.0	23.4
104	742719.808254	2033736.592580	8.3	1558.0	24.5

Table D.2

Electric conductivity field values were taken from Spring Electric conductivity (Rodriguez-Martinez 1997)(Ec) and from spring water samples of the field campaign.

	Ec μS/m	T (C°)	pH	Inst Q f3/s	Latitude	Longitud
Lapileta	370	25.0		0.00	18.391111	-66.662222
Opiola	346			4.00	18.388056	-66.679444
Sumidero	360	25.0	7.5	0.01	18.367778	-66.685000
banbu2	430	23.0	7.5	0.01	18.408056	-66.718889
pvc	450	25.0	7.9	0.00	18.363333	-66.745000
odilioji	700	24.0	7.8	0.00	18.360000	-66.748056
sanrafael	395	27.0	7.7	0.02	18.358333	-66.755833
cambijas	650		7.5	0.00	18.378889	-66.756944
avispa	430	24.0		0.01	18.396667	-66.760556
luispd	460	0.0	8.0	0.00	18.368889	-66.761111
luispu	390	0.0	8.0	0.03	18.369167	-66.761944
ruiz	394	25.0		0.01	18.394167	-66.769444
eligioro	500	24.0	7.7	0.02	18.367500	-66.771111
basilio	740	25.0		0.01	18.394444	-66.773611
aserradero	380	24.0		0.01	18.389444	-66.796944
Publico	318	24.5		0.01	18.404167	-66.801111
riverados	560	27.0		0.01	18.390556	-66.804722
Pozodel muerto	510	26.0		0.01	18.363889	-66.810000

Errata

Section: 3.2.2 Page: 22 Figure 3.1

The caption of Figure 3.1 is as follows:

Figure 3.1 a) Diagram showing the behavior of the primary and secondary fields produced by a naval base and the conductive body respectively b) Zero- crossing points of VLF in-phase components of the secondary magnetic field plot showing positive Fraser filter anomaly indicating possible location of conductive feature.

It should read:

Figure 3.1 a) Diagram showing the behavior of the primary and secondary fields produced by a naval base and the conductive body respectively adapted from ABEM Corporation (1987) b) Zero- crossing points of VLF in-phase components of the secondary magnetic field plot showing positive Fraser filter anomaly indicating possible location of conductive feature adapted from Jones (2007).

Section: 7 Page: 49

Citations added:

ABEM Corporation. 1987. ABEM WADI VLF instrument manual: ABEM, Atlas AB Box 20086 S-161 20 Bromma, Sweden. P.37

Geophysics foundations: Quick overview: Summary of VLF surveying and data [Internet]. 2007. [updated 06/28/2007, cited 15/12/2011] Available from:http://www.eos.ubc.ca/ubcgif/iag/foundations/method-summ_files/vlf-notes.htm